

The Effect of Strain Reversal during High Pressure Torsion on the Evolution of Microstructure, Texture and Hardness Properties of Aluminum Alloys

Kanwal Chadha

A Dissertation Submitted to
Indian Institute of Technology Hyderabad
In Partial Fulfillment of the Requirements for
The Degree of Master of Technology



भारतीय प्रौद्योगिकी संस्थान हैदराबाद
Indian Institute of Technology Hyderabad

Department of Materials Science and Engineering

4th July, 2013

Declaration

I declare that this written submission represents my ideas in my own words, and where others' ideas or words have been included, I have adequately cited and referenced the original sources. I also declare that I have adhered to all principles of academic honesty and integrity and have not misrepresented or fabricated or falsified any idea/data/fact/source in my submission. I understand that any violation of the above will be a cause for disciplinary action by the Institute and can also evoke penal action from the sources that have thus not been properly cited, or from whom proper permission has not been taken when needed.



(Signature)

(Kanwal Chadha)

(MS11M04)

Approval Sheet

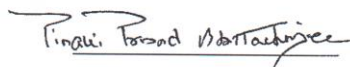
This thesis entitled “The Effect of Strain Reversal during High Pressure Torsion on the Evolution Microstructure, Texture and Hardness Properties of Aluminum Alloys” by Kanwal Chadha is approved for the degree of Master of Technology from IIT Hyderabad.



Dr. Suhash Ranjan Dey
(Department of Materials Science and Engineering)
Examiner



Dr. Bharat Bhooshan Panigrahi
(Department of Materials Science and Engineering)
Examiner



Dr. Pinaki Prasad Bhattacharjee
(Department of Materials Science and Engineering)
Adviser



Dr. Manish Niranjana
(Department of Physics)
Chairman

Acknowledgements

The M.Tech course work at IIT Hyderabad was a great learning experience for me. The thesis work made me learn many new things and made me confident to work on the equipment and explore new ideas. This work would not have executed without the support of many people, who helped me in numerous ways.

I am highly obliged to my guide, Dr. Pinaki Prasad Bhattacharjee, who deeply inspired me throughout this work. With his esteemed guidance and motivation only, I was able to successfully execute the goals for this work.

Also, I am grateful to Prof. H.S Kim, POSTECH, Korea for processing the HPT specimens in his laboratory.

I am thankful to Department of Science and Technology (DST) for their financial support.

My great thank to Mr. J.R. Gatti and Mr. M. Zaid for helping me to conduct experiments and developing my skills to work on intricate equipment single handedly. I would like to thank all faculty members and PhD scholars of Department of Material Science and Engineering for their constant guidance. Also, big thank to my M.Tech colleagues for helping me in course work and spending a great time together.

Lastly, my special gratitude to my parents, Mr. Rakesh Chadha and Mrs. Kiran Chadha and my sister Ms. Vasudha Chadha for their love, guidance and blessings.

Dedicated to

Most Merciful Lord Narsingh Dev

Abstract

The present work aims to investigate the effect of strain reversal during high pressure torsion on the evolution of microstructure, texture and hardness properties of two different materials with different dynamic recovery behavior, namely, high purity Aluminum (>99%, designated as 2N-Al) and Aluminum-Magnesium (Al-2.5%Mg) alloy. For this purpose, 2N-Al and Al-2.5%Mg were subjected to monotonically (CW) and strain reversal (CW-CCW) deformation by High Pressure Torsion (HPT). The samples were subjected to a series of rotations in monotonically and strain reversal deformation with same equivalent strains of 1, 4, 12, 24 and 60 under an applied load of 6 GPa and with 1 rpm under quasi-constrained conditions.

In the two different aluminum alloys subjected to different routes, the evolution of the ultrafine structure follows same trend i.e. initial recrystallized microstructure with large grain size throughout the disk, at low strain level sub grains with prominent LAGBs network inside the grains and ultimately at higher strains ultrafine microstructure throughout the disk characterized by equiaxed grains separated by HAGBs. The only exception to this was observed in case of Al-2.5%Mg during high strains at the center regions where the fraction of HAGBs was found strikingly less as compared to its counterpart during strain reversal deformation. However it was observed that there was no effect on the grain size due to strain reversal for both the alloys, however the fraction of High Angle Grain Boundary (HAGBs) was found lower in case of strain reversal for both the alloys. This phenomenon is related to Bauschinger Effect. Remarkable hardness homogeneity was observed for 2N-Al deformed by both the deformation modes, however the same was not observed for Al-2.5%Mg where the hardness at the center regions was observed to be lesser than the edge regions with exceptionally less hardness at center for strain reversal specimens at higher strains.

The texture evolution ($A/A^- \{1\bar{1}\bar{1}\} < 110 >$ and $\{1\bar{1}1\} < \bar{1}\bar{1}0 >$, $A^*/A^*- \{1\bar{1}1\} < 112 >$ and $\{11\bar{1}\} < 112 >$, $B/B^- \{1\bar{1}2\} < 110 >$ and $\{1\bar{1}\bar{2}\} < \bar{1}\bar{1}0 >$, $C \{001\} < 110 >$ and $(001)[100]$ component) in monotonically deformed 2N-Al revealed a

strong presence of (001)[100] component at lower strains and a mixed texture at higher strains whereas texture evolution in Al-2.5Mg revealed the presence of the C component at lower strains and a mixed texture at the higher strains. The texture evolution in strain reversal deformation in 2N-Al reveals presence of mixed texture at lower strains with dominance of B/B- and A*/A*- components and mixed texture with high presence of the C component at higher strains. In Al-2.5%Mg presence of the A*/A*- component was observed at lower strains whereas as dominance of the C component was observed at higher strains.

Nomenclature

UFG	Ultrafine grained
NS	Nanostructured
HAGB	High Angle Grain Boundary
LAGB	Low Angle Grain Boundary
SPD	Severe Plastic Deformation
HPT	High Pressure Torsion
ϵ	Equivalent Strain Value
CW	Clockwise rotation
CW-CCW	Clockwise followed by Counter Clockwise
2N-Al	99% Pure Aluminum
GB	Grain Boundary
θ_{mis}	Misorientation of Grain Boundaries
EBSD	Electron Back Scatter Diffraction
PF	Pole Figure
ODF	Orientation Distribution Function
A/A ⁻	$\{1\bar{1}\bar{1}\} \langle 110 \rangle$ and $\{\bar{1}11\} \langle \bar{1}\bar{1}0 \rangle$
A*/A*-	$\{\bar{1}\bar{1}1\} \langle 112 \rangle$ and $\{11\bar{1}\} \langle 112 \rangle$
B/B ⁻	$\{\bar{1}12\} \langle 110 \rangle$ and $\{1\bar{1}\bar{2}\} \langle \bar{1}\bar{1}0 \rangle$
C	$\{001\} \langle 110 \rangle$
FCC	Face Centered Cubic

Contents

Declaration.....	ii
Approval Sheet	Error! Bookmark not defined.
Acknowledgements.....	iv
Abstract.....	vi
Nomenclature	viii
1 Intrduction	1
1.1 Overview.....	1
1.2 Objective and Scope.....	4
2 Literature Review	5
2.1 Evolution of microstructure and texture during HPT processing	5
2.2 The effect of strain path change.....	7
3 Experimental Procedure	9
3.1 Preparation of disks for HPT.....	9
3.2 High Pressure Torsion Processing.....	10
3.3 Characterization.....	10
3.3.1 Hardness test of processed HPT disks.....	10
3.3.2 Microstructure and Texture Characterization	11
4 Results	12
4.1 Starting materials microstructure of 2N-Al.....	12
4.2 HPT processed specimens.....	12
4.2.1 Microstructure Evolution.....	12
4.2.2 Micro-texture Evolution.....	16
4.2.3 Microhardness Properties.....	20
5 Results	22
5.1 Starting materials microstructure of Al-2.5Mg.....	22
5.2 HPT processed specimens.....	22
5.2.1 Microstructure Evolution.....	22
5.2.2 Micro-texture Evolution.....	27
5.2.3 Microhardness Properties.....	32

6 Discussion	34
6.1 Evolution of microstructure and hardness properties.....	34
6.2 Evolution of Texture.....	38
7 Conclusions	45
References	47

Chapter 1

Introduction

1.1 Overview

Development of high strength structural materials through grain size reduction as conceived in the Hall-Petch relation ($\sigma_y = \sigma_0 + kd^{-1/2}$) [1] has been a major driving force in the fabrication of Ultrafine Grained (UFG with grain size $<1\mu\text{m}$) and Nanostructured (NS with grain size $<100\ \mu\text{m}$) materials with large fraction of high angle grain boundaries (HAGBs). Fabrication of UFG and NS can be achieved by two methods, bottom up technique and top down approaches. Bottom Up fabrication is done through synthesis and consolidation individual atoms or Nano particles solids, such as, electro deposition [2], inert gas condensation [3] and ball milling followed by subsequent consolidation [4]. Despite the fact that these methods have the capability to produce very small grain size, they suffer from disadvantages such as small size of the finished product, often residual porosity.

These disadvantages may be completely overcome in Top Down approach in which bulk solid with coarse grain size is processed by imposing high strain in order to refine the grain size to submicrometer size.

Severe Plastic Deformation (SPD) is the most well-known top down approach for fabrication UFG and NS materials. Fabrication of materials by SPD is usually done by imposing very high plastic strain, without concomitant changes in the dimensions of the work pieces. SPD techniques such as Equi Channel Angular Processing (ECAP) [5], Accumulative Roll Bonding (ARB) [6] and High Pressure Torsion (HPT) [7] can now successfully produce wide variety of bulk Ultra Fined Grained and Nano structured materials.

Amongst various SPD processing technique HPT has gained significant attention due to fact that large plastic strain value can be easily achieved in this process. The sample in the form of thin disc is placed between two anvils and a very high compressive load is applied with simultaneous torsion strain (Fig 1.1c)

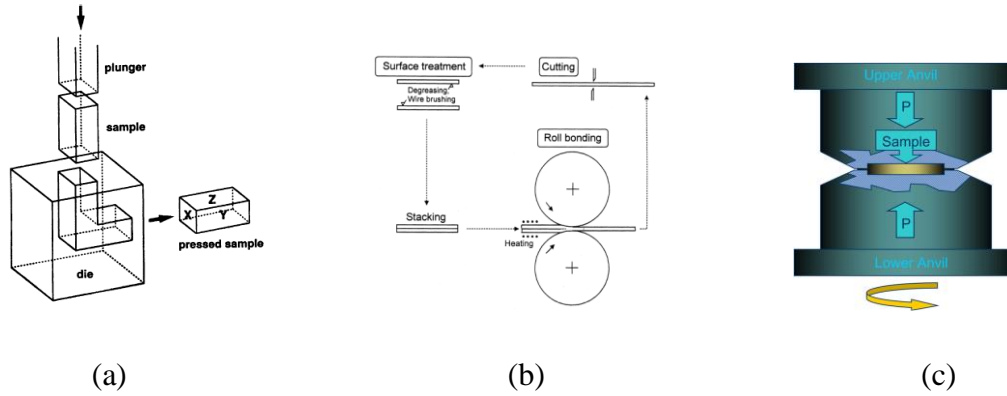


Fig 1.1: S.P.D processes (a) ECAP [5], (b) ARB [6] and (c) HPT [7]

The equivalent strain value in HPT can be calculated by:

$$\epsilon \approx \frac{1}{\sqrt{3}} \frac{r}{h} \varphi$$

Where r = radius of the disc in mm, h = height of disc in mm, φ = angle of rotation in radians and ϵ = equivalent strain value.

According to the equation the strain is directly proportional to the radius of the disc which indicates that at the center the strain is ideally zero whereas the strain is highest at the edges of the disc (Fig.1.2). This strain inhomogeneity can be overcome by imposing very high strain values by increasing the number of rotations [8].

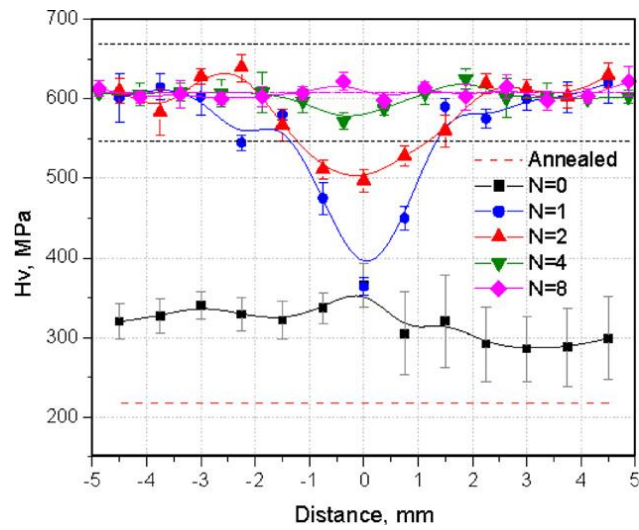


Fig 1.2: Microhardness distributions across the diameters of aluminum discs subjected to HPT at a pressure of $P=1\text{GPa}$ and up to eight turns. [7]

While the development of microstructure and mechanical properties have been intensely investigated the evolution of texture is only the beginning to be studied. It is expected that level of strain and strain path change should strongly effect the formation of texture as observed for conventional deformation processing and also shown very recently for HPT processing [8, 9].

The stain path change during HPT can be easily achieved by monotonous and reversal strain deformation through the combination of clockwise (CW) and subsequent anticlockwise rotation (CW-CCW) (Fig.1.3). The present study attempts to comprehensively study the effect of strain and strain path change on the formation of microstructure, texture and properties during HPT processing.

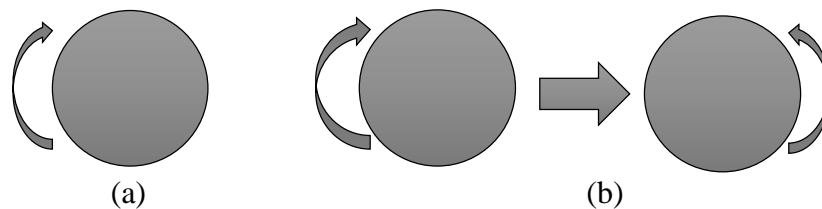


Fig 1.3: Type of deformation by HPT: (a) Monotonic Deformation (b) Strain Reversal deformation.

1.2 Objective and Scope:

The present work aims to investigate the effect of strain path change on the evolution of microstructure, texture and hardness properties of two different materials with different dynamic recovery behavior, namely, high purity Aluminum (>99%, designated as 2N-Al) and Aluminum-Magnesium (Al-2.5%Mg) alloy. It is envisaged that strain reversal would greatly affect the microstructure-texture-property evolution in materials with different dynamic behavior which essentially remains the main motivation for the present study.

Chapter 2

Literature Review

2.1 Evolution of microstructure and texture during HPT processing

The pioneering works by Bridgman lead to the origin of metals processing by HPT [7]. Prof. Bridgman won Nobel Prize in Physics for his extensive research on Physics of High Pressure.

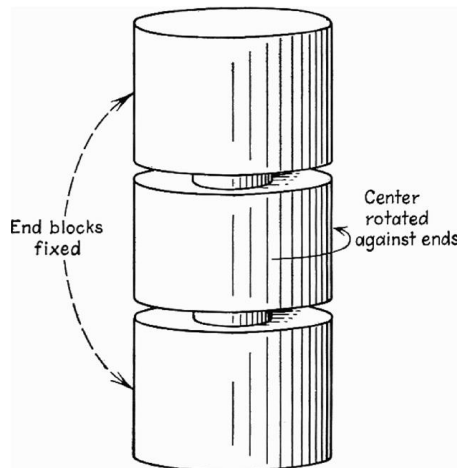


Fig 2.1: General schematic of the apparatus used by Bridgman in which torsional straining is combined with longitudinal compression [7].

Extensive research has been conducted on aluminum alloys to investigate the effect of HPT on the evolution of microstructure and mechanical properties [10, 11, 12, and 13].

The investigations on the HPT processing indicate that there is increase in the hardness with the increase in the strain or the number of rotations and at high strain values, the hardness homogeneity is achieved. It is generally observed that HPT processing leads to development of ultrafine grains at high strain levels separated by high angle grain boundaries (HAGBs).

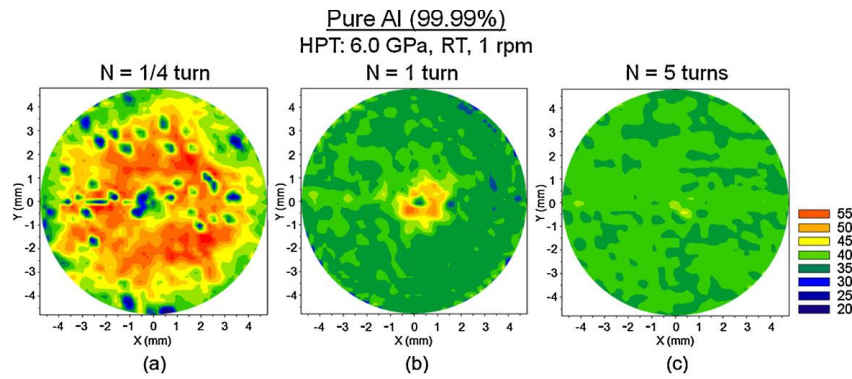


Fig.2.2 Color Coded hardness contour maps for 99.99% aluminum after (a) $\frac{1}{4}$, (b) 1 and (c) 5 turns. [10]

In contrast texture studies on HPT materials are rather limited and have been carried out by few researchers only [14, 15]. Torsion texture development in F.C.C. metals are labeled $\{hkl\}\langle uvw \rangle$, where $\{hkl\}$ is a plane parallel to the shear plane and $\langle uvw \rangle$ is the shear direction Θ . Four types of ideal orientations are observed.

(A) $\{\bar{1}\bar{1}\bar{1}\}\langle 110 \rangle$ and $\{\bar{1}11\}\langle \bar{1}\bar{1}0 \rangle$

(A*) $\{\bar{1}\bar{1}1\}\langle 112 \rangle$ and $\{11\bar{1}\}\langle 112 \rangle$

(B) $\{\bar{1}\bar{1}2\}\langle 110 \rangle$ and $\{1\bar{1}\bar{2}\}\langle \bar{1}\bar{1}0 \rangle$

(C) $\{001\}\langle 110 \rangle$

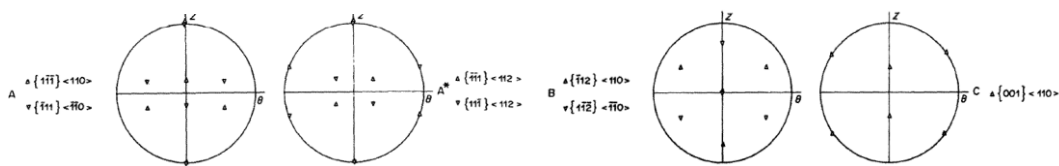


Fig 2.3: Four types of ideal orientations during the torsion testing of fcc aluminum and copper $\{111\}$ poles. [15]

The studies reveal that A component $\{\bar{1}\bar{1}\bar{1}\}\langle 110 \rangle$ dominates in lower strains whereas the C component $\{001\}\langle 110 \rangle$ dominates at higher strain values.[15] The same results have been reported in D. Orlov et al. During monotonous deformation, at strain of $\epsilon=1$, A fiber dominates while at strain $\epsilon=4$, C fiber dominates.

But as the strain is increased, the texture becomes weak and randomized. Minor presence of A* and B fiber was also observed. [9]

2.2 The effect of strain path change

Strain path change during deformation processing greatly impacts the microstructure, texture and mechanical properties of materials. Very recently, strain path change during cold rolling has demonstrated significant variation in texture and microstructure from straight cold rolling [8].

Strain reversal during HPT on the evolution of hardness and microstructure has been reported by few researchers. It has been reported that disc subjected to strain reversal show limited increase in the hardness at the center with increasing strain values, which is justified upon microstructure observation at the center where grain refinement is limited[16]. Similar results have been reported in another study, that strain reversal retards the formation of HAGBs and thereby less grain refinement [17].

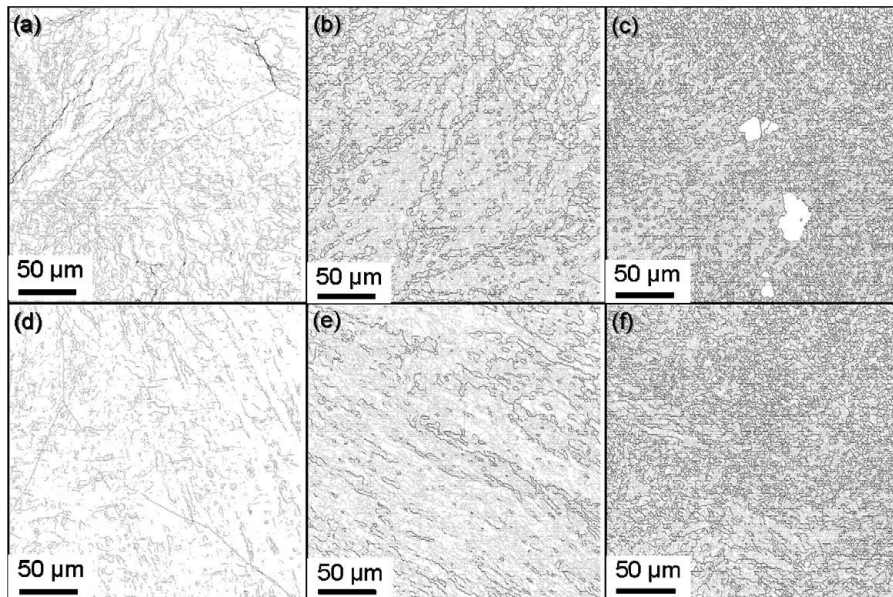


Fig2.4: Grain Boundary maps of 4N-Al after HPT processing. The maps a, b and c correspond to monotonic straining to 96° rotation; d, e and f correspond to 4 cycles of reversal straining with amplitude of $\pm 12^{\circ}$. The maps a and d, b and e, c and f were obtained at specimen's axis, middle radius and edge respectively. HAGBs are in black color and LAGBs are in grey. [17]

Development of texture due to the effect of strain reversal has been investigated to a very less extent. D. Orlov et al investigated on the development of texture during monotonic and strain reversal in high purity aluminum [9]. It is reported that there is development of A fiber in both deformation modes at lower strain levels whereas at higher strain levels, C component becomes dominant in monotonic deformation and (001) [100] becomes dominant in strain reversal deformation.

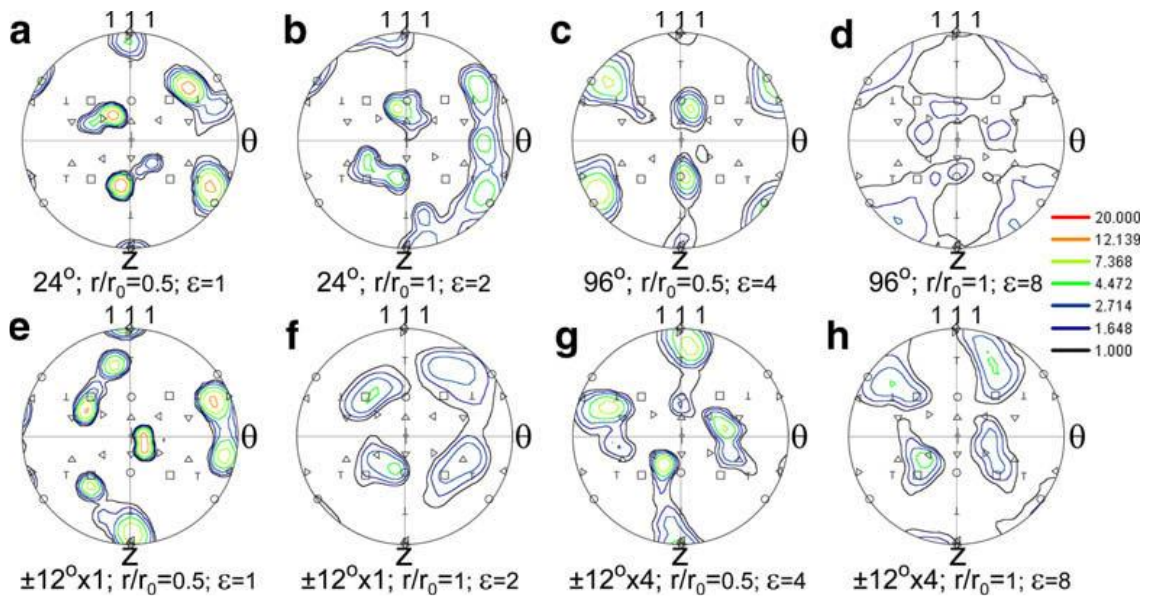


Fig 2.5: (111) Pole figures of 99.99% Al after monotonous (a-d) and strain reversal (e-h) deformation constructed from the EBSD data. [9]

The present literature review shows that the strain reversal during HPT processing significantly impacts the evolution of microstructure, texture and hardness properties of materials. But till date till date no study has been done in order to compare different materials with different dynamic recovery behavior subjected to both monotonic and strain reversal deformation during HPT processing, which is the major focus of the present work.

Chapter 3

Experimental Procedure

3.1 Preparation of Disks for HPT

2N-Al and Al-2.5%Mg alloy were used for the present study. 2N-Al was received in the form of fully annealed plates of approximately 2mm thickness. The as-received Al-2.5%Mg block (160mm(length) × 60mm (width) × 10mm (thickness)) was cold rolled to ~80% reduction in thickness and annealed in air furnace at 673K for one hour. The above two materials were used as the starting materials for further processing.

Disks with the diameter of 10mm were then cut from the sheet using EDM wire cut equipment. A total of 10 disks of each alloy were cut for further HPT processing. These disks having 2.5mm starting thickness were manually grinded to ~1.5mm thickness using SiC grit papers with grit size of 500, 1000 and 1200 respectively. The disks were then designated according to the strain value or the number of rotations as per the given chart.

Table 3.1: Designation of the samples according to the strain

Monotonic	Strain Reversal	Equivalent Strain
CW 30°	CW(15°)-CCW(15°)	1
CW120°	CW(60°)-CCW(60°)	4
CW 1R	CW(180°)-CCW(180°)	12
CW 2R	CW(1R)-CCW(1R)	24
CW 5R	CW(2.5R)-CCW(2.5R)	60

CW- Clockwise Rotations, CW-CCW – Clockwise followed by counter clockwise

3.2 High Pressure Torsion Processing

The disks were then deformed by HPT to the desired strain levels. The imposed load was fixed at 390KN (~5GPa) and a rotation speed of 1 rpm was used at quasi-constrained conditions [18]. The processing of the disks were done at POSTECH, South Korea in the group of Prof. H.S. Kim. The schematic diagram for HPT processing is shown in Fig: 3.1.

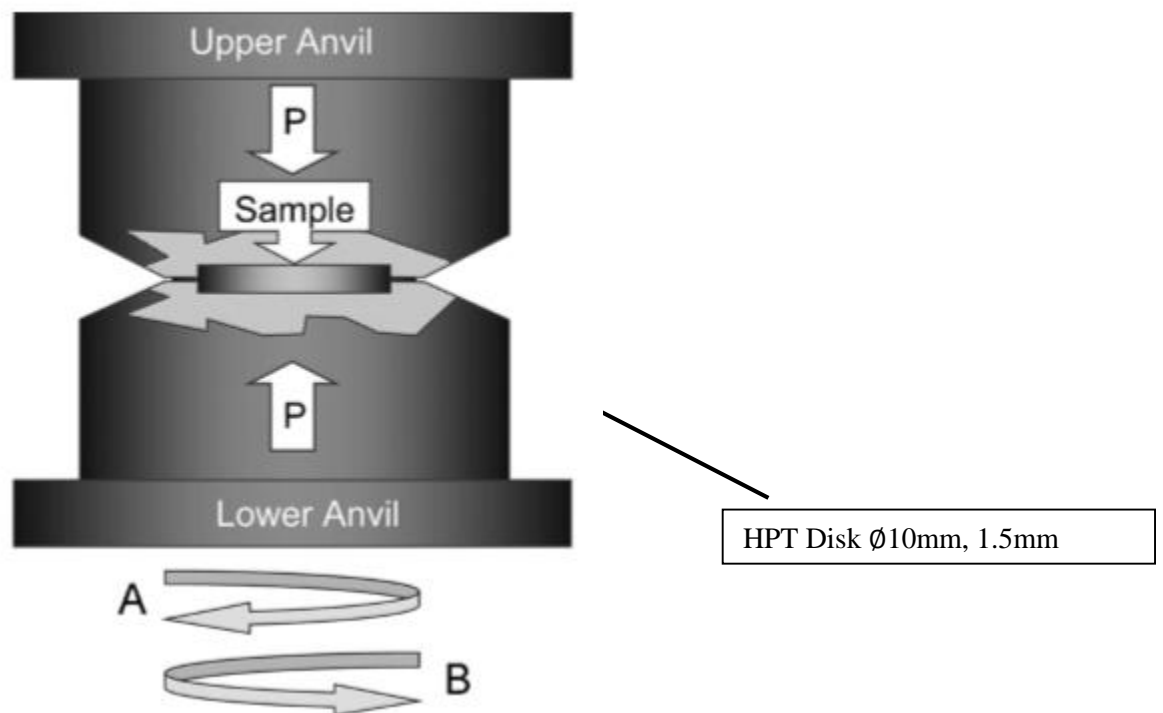


Fig 3.1: Schematic illustration of HPT processing with strain reversal processing capability. [19]

3.3 Characterization

3.3.1 Hardness test of processed HPT disks

To measure the hardness variation across the disk, Vickers microhardness test (Make: EMCO-TEST, Austria; Model: Dura Scan-70) was conducted on the disks. The disks were mounted using Hot Mounting Equipment (Make: Struess Citupress-

10) and then manually grinded and polished in order to obtain a mirror finish. To measure hardness variation precisely, microhardness indentation points were taken 0.5mm apart from each other on two mutually perpendicular diameters of the disk under conditions of applied load of 200g with a dwell time of 15sec.

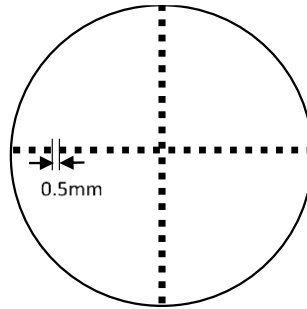


Fig 3.2: Schematic illustration of microhardness measurements across the HPT disk.

3.3.2 Microstructure and Texture Characterization

The microstructure and texture of the processed HPT disks were characterized by Electron Back Scattered Diffraction (EBSD) attached to a FEG-SEM (Make: Carl Zeiss; Model Supra 40) using Channel 5™ Software (Oxford Instruments, UK). EBSD measurements were taken on the r - θ plane of disks at center, middle and edge region of the disks as illustrated schematically in the Fig 3.3(b). For EBSD investigations, the sample were polished mechanically using SiC paper of grit size 2000, followed by electropolishing using a mixture of perchloric acid and ethanol as electrolyte (1:9) at 20V and -30°C (using Liquid N_2) for 20 sec. The microtexture analysis was done by assuming triclinic sample symmetry.

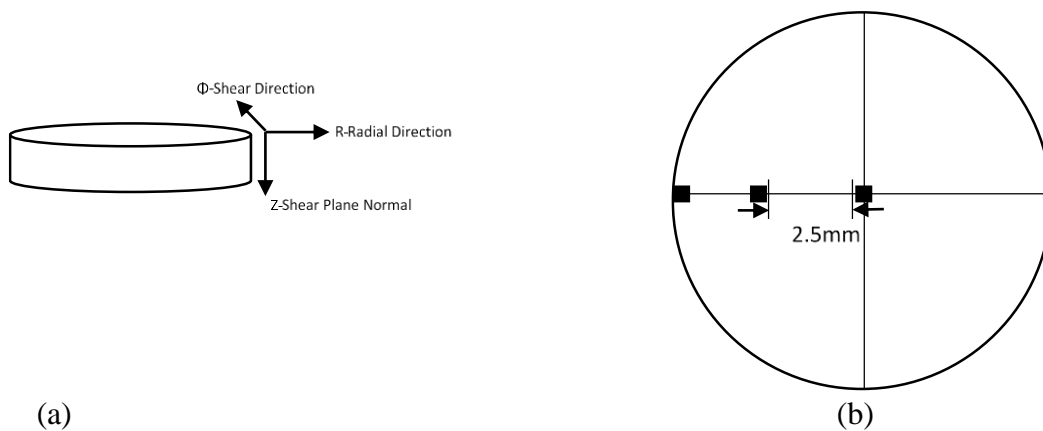


Fig 3.3: Schematic illustration of (a) Sample geometry, (b) EBSD measurements areas.

Chapter 4

4.1 Starting Material microstructure of 2N-Al

Fig. 4.1 shows the microstructure of 2N-Al starting material. The high angle grain boundaries HAGBs having misorientation ($\theta_{\text{mis}} \geq 15^\circ$) are highlighted in black and low angle grain boundaries LAGBs with misorientation ($15^\circ \geq \theta_{\text{mis}} \geq 2^\circ$) are highlighted in red. The average grain size is $\sim 28\mu\text{m}$ and fraction of HAGBs is found to be 74%. The starting microstructure reveals typical recrystallized microstructure.

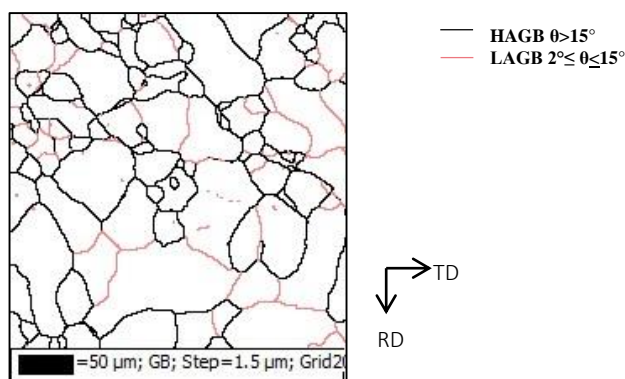


Fig. 4.1: Microstructure graph of 2N-Al starting material

4.2 HPT processed specimens

4.2.1 Microstructure Evolution

The grain boundary (GB) maps of the samples deformed by different deformation modes are shown in Fig. 4.2 and Fig. 4.3. Fig. 4.2 shows microstructures of monotonically deformed specimens while Fig. 4.3 shows microstructures of strain reversal specimens, respectively. The variation in the average grain size and fraction of HAGBs with imposed strain are plotted in Fig. 4.4 (a,c) for monotonically deformed specimens and in Fig. 4.4 (b,d) for strain reversal specimens.

After $\epsilon=1$ (CW 30°), Fig. 4.2 (a, f, k), the microstructure consists of starting recrystallized grains but inside the starting recrystallized grains LAGBs network can be easily observed. The structure at the center remain coarse at $\epsilon=4$ (CW 120°), but a much finer structure is observed at the middle and edge regions. Further deformation upto $\epsilon=12$ (CW 1R), refines the microstructure at both the middle region so that equiaxed microstructure could be observed at both these regions. However, the microstructure at the center region continues to demonstrate the rather coarse appearance. Deformation beyond this level (at $\epsilon=24$ (CW 2R) and $\epsilon=60$ (CW 5R)) results in the evolution of an ultrafine microstructure at the middle and the edge regions characterized by rather equiaxed grains separated by HAGBs. The center regions even at this deformation level is not refined and appear strikingly dissimilar as compared to the middle and edge regions.

Fig. 4.3 show the GB maps of strain reversal specimens at different strain level. The microstructure evolution for middle and edge region appears very similar for both the deformation modes such that at lower strains the structure consist of huge fraction of LAGBs and with increasing strain gradually transforms into an ultrafine-grained structure. However at the center region in case of strain reversal specimens (Fig. 4.3 (a-e)), the microstructure evolution is remarkably different from monotonically deformed specimens. At the center after $\epsilon=12$ (CW(180°)-CCW(180°)), the microstructure is already found to be refined significantly with high fraction of HAGBs. Beyond this deformation level (at $\epsilon=24$ (CW(1R)-CCW(1R)) and $\epsilon=60$ (CW(2.5R)-CCW(2.5R))) the center regions demonstrate the evolution of an ultrafine grained structure characterized by equiaxed grains separated by HAGBs.

The evolution of key microstructural parameters such as average grain size and HAGB fraction is shown in Fig.4.3. It can be inferred from Fig. 4.4 (a) for monotonous deformed specimens that after HPT processing, the average grain size decreases. The average grain size at the center when 30° clockwise rotation was imposed on the disk decreases from $28\mu\text{m}$ (starting material) to $26\mu\text{m}$. The average grain size continuously decreases at the center, middle and the edge as the number of rotations increases. The average grain size at the edge reduces from $\sim 3.6\mu\text{m}$ after 30° clockwise rotation to 370nm after 5 full rotations. The average grain size after 1 and

2 full rotations at the middle and the edge is very similar. However the average grain size at the center reduces at a relatively slower rate and after 5 rotations it reduces to $\sim 3.3\mu\text{m}$. The fraction of HAGBs Fig. 4.4 (c), in case of center and middle increases from 14% and 13% after 30° clockwise rotation to 32% and 85% after 5 full rotations respectively. In case of the edge the fraction of HAGBs first increase drastically to 80% after 120° clockwise rotations and then reduce to 47% after 1 rotation and thereafter increases to 83% after 5 rotations.

During strain reversal deformation (Fig. 4.4(b)) after 30° clockwise-counter clockwise (CW(15°)-CCW(15°))rotation, the average grain size decreases from $\sim 28\mu\text{m}$ to $\sim 4\mu\text{m}$ in edge region. The average grain size at the center also reduces to $\sim 27\mu\text{m}$. The Average grain size continuously reduces at center, middle and edge region from $\sim 19\mu\text{m}$, $\sim 14\mu\text{m}$ and $\sim 4\mu\text{m}$ after 30° strain reversal ((CW(15°)-CCW(15°))) rotation to $1.3\mu\text{m}$, $1.2\mu\text{m}$ and $1.1\mu\text{m}$ after 5 strain reversal rotations (CW(2.5R)-CCW(2.5R)). After 5 strain reversal (CW(2.5R)-CCW(2.5R)) rotations, it can be noted that the grain size is almost similar thus signifying remarkable homogeneity across the disk. HAGBs fraction (Fig. 4.4 (d)) increases from 31% at edge region after 30° strain reversal (CW(15°)-CCW(15°))to 86% after 2 turns (CW-CCW 1 turn). Thereafter no significant change is observed and the HAGBs remains almost unchanged up to 5 turns (CW-CCW 2.5). In case of center region, the HAGBs first decrease after 120° strain reversal (CW-CCW 60°) and then increase. After 5 turn strain reversal deformation (CW-CCW 2.5), fraction of HAGBs at center, middle and edge shows very similar values.

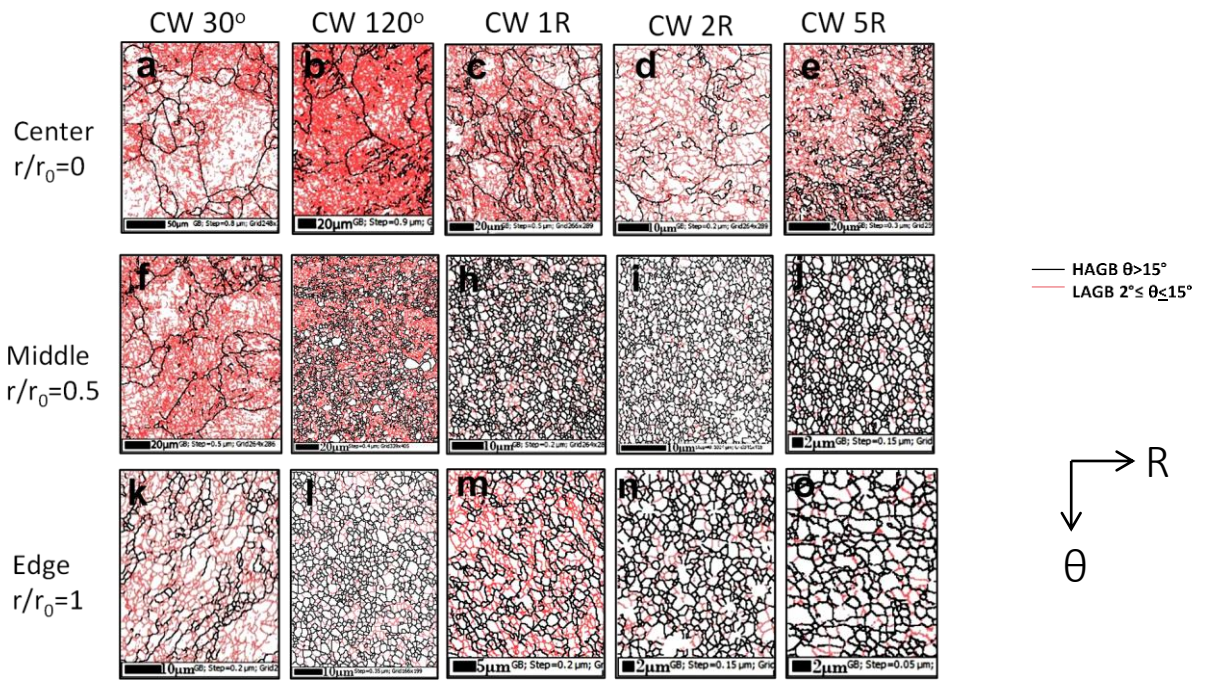


Fig. 4.2: Grain boundary maps of monotonically deformed 2N-Al processed to different strain levels; center ($r/r_0=0$) (a-e), middle ($r/r_0=0.5$) (f-j) and edge regions ($r/r_0=1$) (k-o).

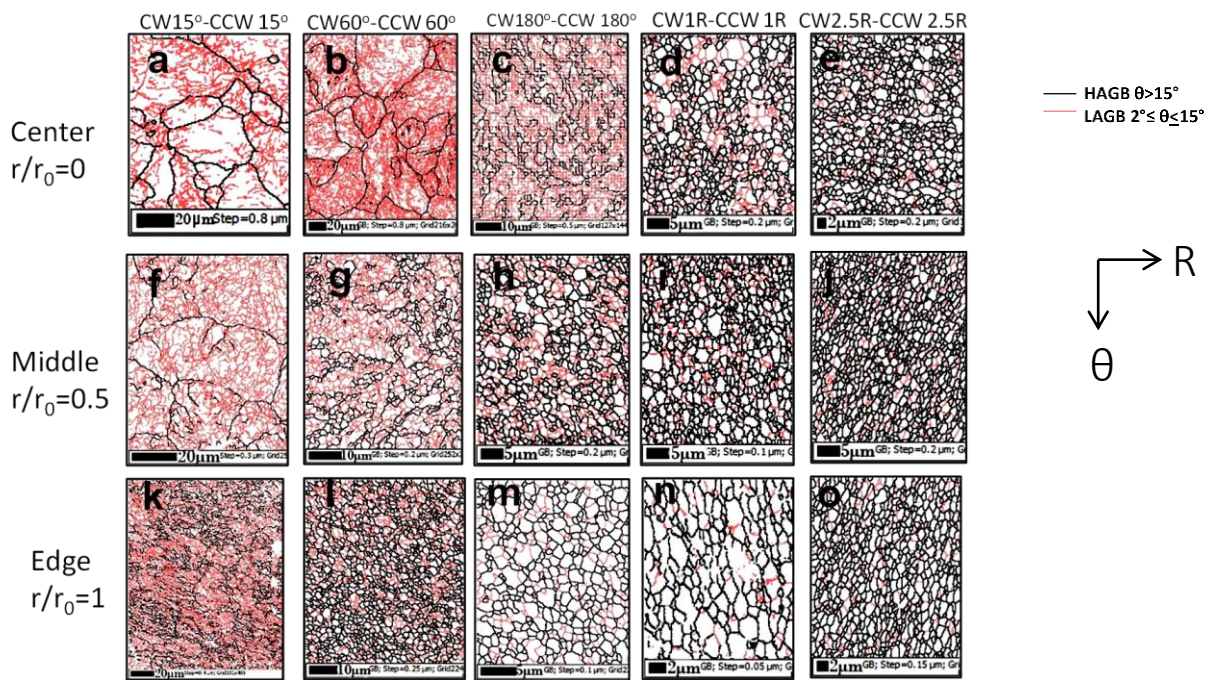
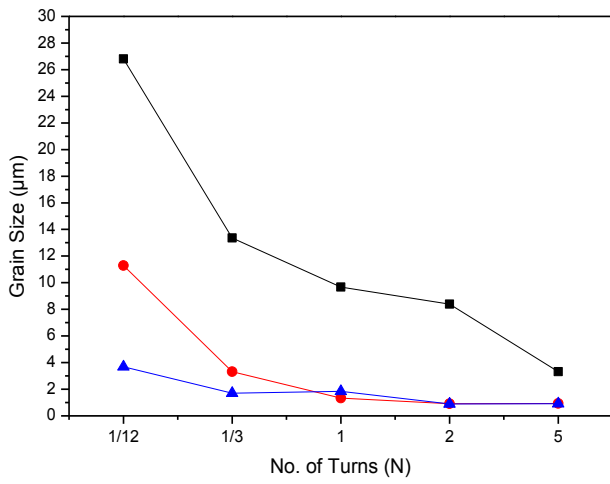
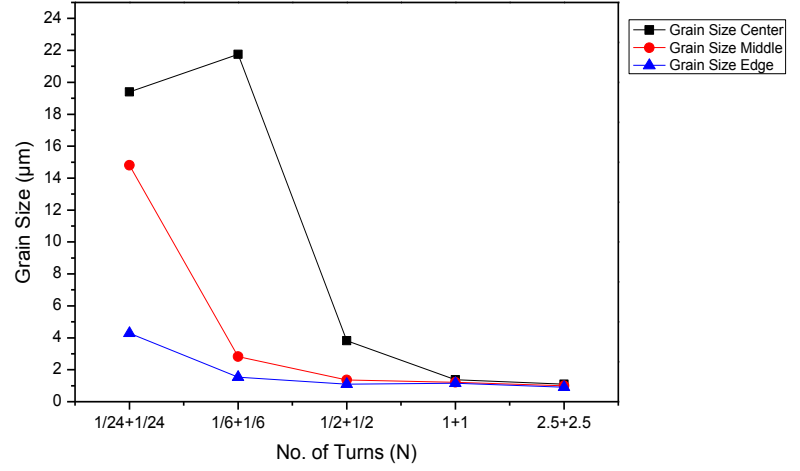


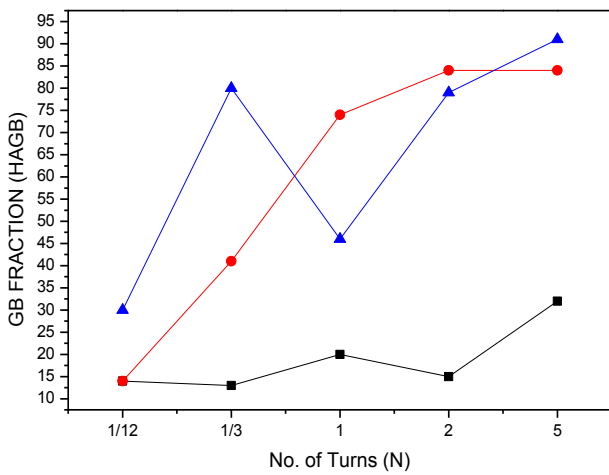
Fig. 4.3: Grain boundary maps of strain reversal deformed 2N-Al processed to different strain levels; center ($r/r_0=0$) (a-e), middle ($r/r_0=0.5$) (f-j) and edge regions ($r/r_0=1$) (k-o).



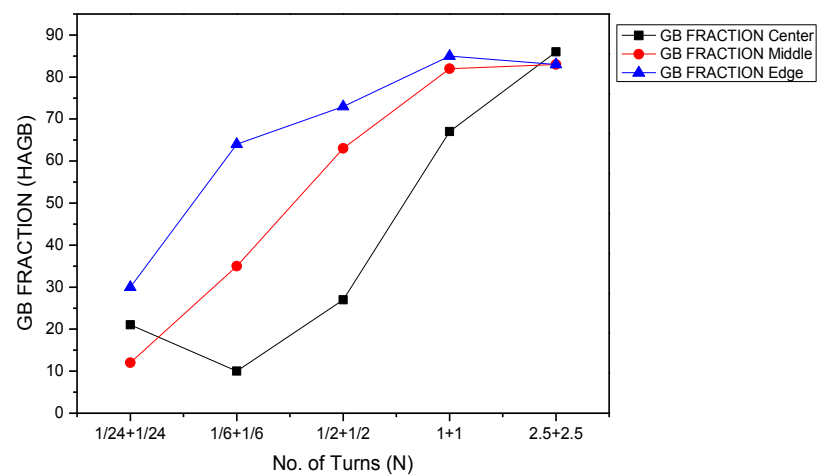
(a)



(b)



(c)



(d)

Fig. 4.4: Variation of grain size ((a),(b)) and HAGB fraction ((c),(d)) with imposed strain in monotonous ((a),(c)) and strain reversal deformation ((b),(d)) modes.

4.2.2 Micro-texture Evolution

Figure 4.5 shows the (111) pole figure for the monotonically (a-e) and strain reversal deformed specimens (f-j). Figure 4.6 shows the $\Phi_2=45^\circ$ section of the ODF of monotonic ((a)-(e)) and strain reversal deformed specimens ((f)-(j)). Fig 4.7 shows the orientation maps depicting the spatial distribution of different texture components

for the monotonically ((a)-(e)) and strain reversal deformed specimens ((f)-(j)). Only the edge regions has been considered here as the maximum strain is obtained at the edge of the specimen in the torsional geometry. The ideal shear texture components are shown in (111) pole figure in Fig. 4.5-(k). Torsion texture development in F.C.C. metals are labeled $\{hkl\}\langle uvw \rangle$, where $\{hkl\}$ is a plane parallel to the shear plane and $\langle uvw \rangle$ is the shear direction Θ [14]. The ideal shear texture components are listed in Table 1. [15]

During monotonous deformation, at $\varepsilon = 1$ (Fig. 4.5 (a), Fig 4.6(a)) a strong presence of the (001)[100] fibre can be observed having a volume fraction of $\sim 18\%$ (Fig. 4.7(a)). Other components are present only in negligible proportion. At $\varepsilon = 4$ (Fig.4.5(b), Fig4.6(b)), the strong presence of the C component having a volume fraction of $\sim 15\%$ along with considerable presence of A/A^- fibre ($\sim 6\%$) can be observed (Fig 4.7 (b)). At $\varepsilon = 12$ (Fig.4.5(c), Fig. 4.6(c)), a noticeable presence of (001)[100] can be seen with a volume fraction of $\sim 9\%$. Significant presence of A/A^- fibre with the volume fraction of $\sim 10\%$ (Fig. 4.7(c)) can also be observed. At $\varepsilon = 24$ (Fig. 4.5(d), Fig. 4.6(d)), strong presence of the C component having the volume fraction of $\sim 12\%$ (Fig 4.7 (d)) can be observed. The volume fraction of A/A^- and A^*/A^{*-} decreases to $\sim 3.5\%$ at this strain level. At $\varepsilon = 60$ (Fig 4.5(e), Fig 4.6 (e), Fig. 4.7(e)), the presence of the C, B/B^- , A^*/A^{*-} and A/A^- fibre can be seen with the volume fraction between $\sim 6-8\%$.

During strain reversal deformation, at $\varepsilon = 1$ (Fig. 4.5 (f), Fig. 4.6(f)), presence of the B/B^- fibre can be observed with the volume fraction of $\sim 9\%$ (Fig.4.7 (f)). A^*/A^{*-} fibre is also observed at this strain level with the volume fraction of $\sim 8\%$. At $\varepsilon = 4$ (Fig. 4.5 (g), Fig. 4.6(g)), presence of the A/A^- is noticed having the volume fraction of $\sim 9\%$ (Fig.4.7 (g)). Presence of the C component is increased to $\sim 6\%$. With the increase in strain at $\varepsilon = 12$ (Fig. 4.5 (h), Fig. 4.6(h)), a strong presence of the C component can be observed having the volume fraction of $\sim 13\%$ (Fig. 4.7(h)). The A/A^- fibre can also be observed at this strain having the volume fraction of $\sim 10\%$. At $\varepsilon = 24$ (Fig. 4.5 (i), Fig. 4.6(i)), the strength of the C and A^*/A^{*-} fibre decreases to $\sim 7\%$ which is confirmed in the corresponding orientation map (Fig.4.7 (i)). After an imposed strain of $\varepsilon = 60$ both the pole figure (Fig. 4.5 (j)) and the ODF (Fig. 4.6(j))

reveal weak intensities thereby confirming weakening of the texture. The corresponding orientation map (Fig. 4.7 (i)) confirms the same which shows the fraction of the C, A*/A*⁻ and A/A⁻ fibre found to be similar lying between 5-6%.

The texture evolution in 2N-Al subjected to the two different processing routes is summarized in Figures 4.8(a) and 4.8(b) for monotonically and strain reversal deformed specimens.

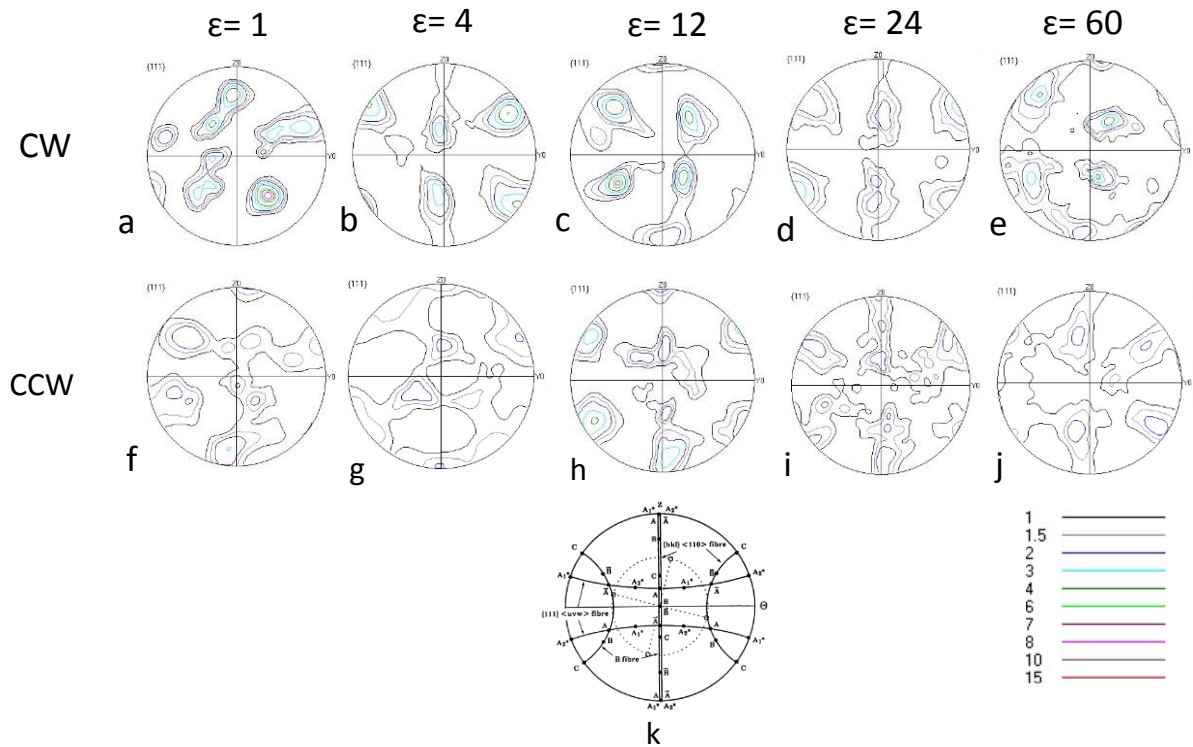


Fig. 4.5: (111) pole figure of the edge regions of monotonically (a-e) and strain reversal (f-j) specimens. The ideal texture components in (111) pole figure is shown in (k) [20].

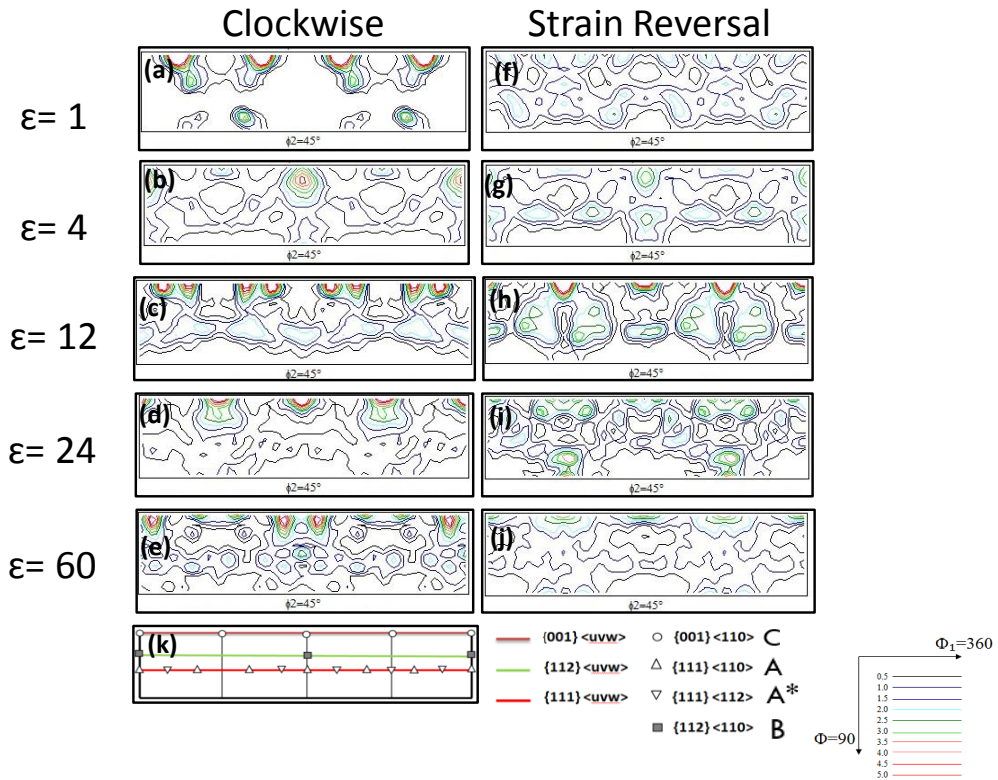


Fig. 4.6: $\Phi_2=45^\circ$ sections of the ODFs of monotonically (a-e) and by strain reversal (f-j) deformed obtained from the edge region ($r/r_0=1$). The ideal positions of ideal shear texture components is shown in (k) [21].

Table 1: Ideal texture components for fcc metals

Component	$\{hkl\}\langle uvw \rangle$
A	$\{1\bar{1}\bar{1}\}\langle 110 \rangle$
A-	$\{\bar{1}11\}\langle \bar{1}\bar{1}0 \rangle$
A*	$\{\bar{1}\bar{1}1\}\langle 112 \rangle$
A*-	$\{11\bar{1}\}\langle 112 \rangle$
B	$\{\bar{1}12\}\langle 110 \rangle$
B-	$\{1\bar{1}\bar{2}\}\langle \bar{1}\bar{1}0 \rangle$
C	$\{001\}\langle 110 \rangle$

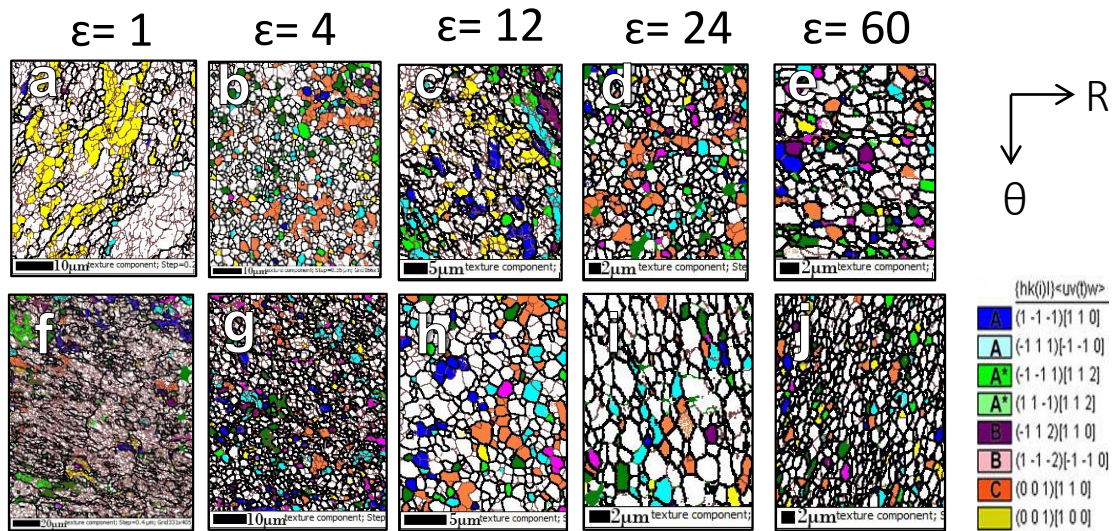


Fig. 4.7: EBSD maps of monotonically (a-e) and strain reversal deformed specimens (f-j).

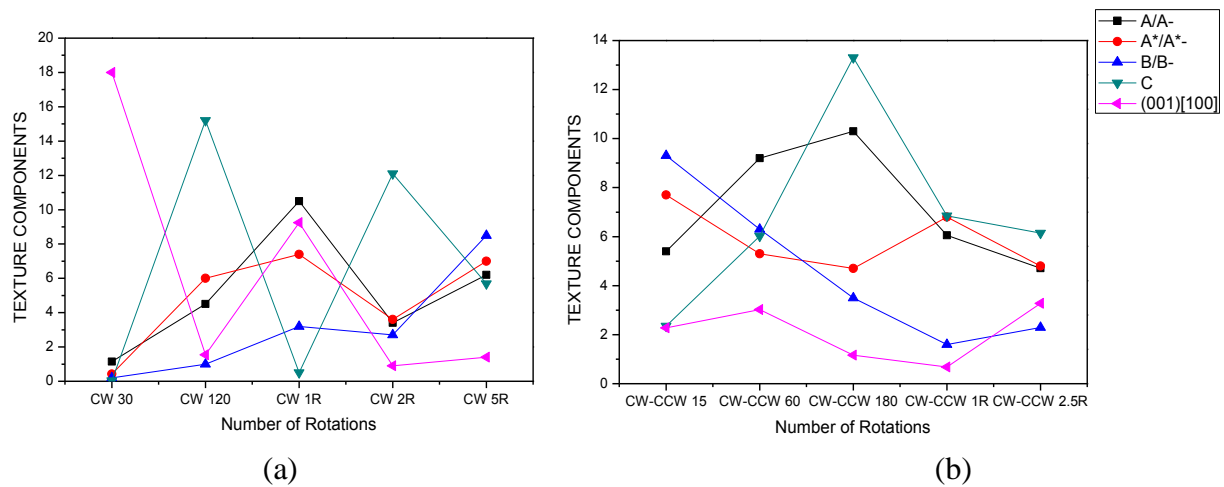


Fig. 4.8: Variation of texture component with imposed strain for (a) monotonically (b) strain reversal deformed specimens.

4.2.3 Microhardness Properties

The distribution of hardness values across the diameters are shown in Fig. 4.9 for the disks processed by HPT through monotonous (CW) and strain reversal (CW-CCW) deformation mode. The lower straight line shows hardness value of $H_v=28$ of the annealed starting material used for further HPT processing.

The hardness values of the monotonically and strain reversal deformed specimens at the lower strain levels are found to be very similar and shows very similar distribution characterized by higher hardness values at the edge and minimum at the center which is typical for the HPT processed disks. At the highest strain $\epsilon=60$, the difference in the hardness values is quite apparent. The hardness of the strain reversal specimen is observed to be higher than monotonically deformed specimens. The hardness at the edge region of the monotonically deformed specimens is ~ 53 whereas in case of strain reversal deformed is ~ 57 . The hardness value at the center region of the strain reversal specimen is ~ 53 and that of monotonically deformed specimens is ~ 47 . It can be thus clearly seen that the hardness value across the disk of strain reversal deformed specimens at higher strain is greater as compared to the hardness values of monotonically deformed specimens. It can be clearly seen that the hardness homogeneity is achieved at highest strain level.

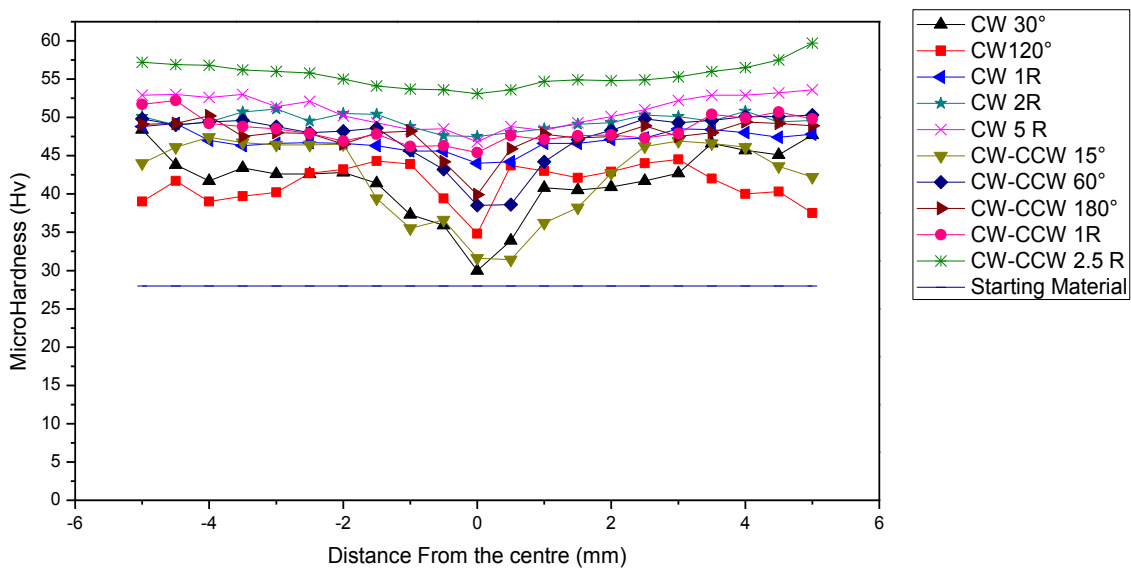


Fig. 4.9: Hardness distribution in monotonically and strain reversal deformed specimens at different strains.

Chapter 5

5.1 Starting Material microstructure of Al-2.5Mg

Fig 5.1 shows the microstructure of Al-2.5Mg starting material. The high angle grain boundaries HAGBs having misorientation ($\theta_{\text{mis}} \geq 15^\circ$) are highlighted in black and low angle grain boundaries LAGBs with misorientation ($15^\circ \geq \theta_{\text{mis}} \geq 2^\circ$) are highlighted in red. The average grain size is $\sim 31\mu\text{m}$ and fraction of HAGBs is found to be 68%. The starting microstructure reveals typical recrystallized microstructure.

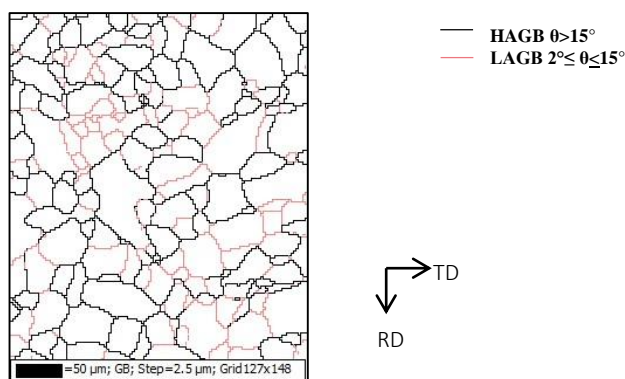


Fig 5.1: Microstructure graph of Al-2.5Mg starting material

5.2 HPT processed specimens

5.2.1 Microstructure Evolution

The grain boundary (GB) maps of the samples deformed by different deformation modes are shown in Fig 5.2 and Fig 5.3. Fig 5.2 shows microstructures of monotonically deformed specimens while Fig 5.3 shows microstructures of strain reversal specimens, respectively. The variation in the average grain size and fraction of HAGBs with imposed strain are plotted in Fig 5.4 (a,c) for monotonically deformed specimens and in Fig 5.4 (b,d) for strain reversal specimens.

After $\epsilon=1$ (Fig 5.2-(a, f, k)), the microstructure consists of mostly sub grains with prominent LAGB network inside the grains. The structure at the center and middle regions essentially remain coarse at $\epsilon=4$ but a much finer structure is observed at the edge region. The microstructure at the middle and center regions, however, remain visibly coarse. Further deformation up to $\epsilon=12$ refines the microstructure at the middle region so that a rather equiaxed microstructure is observed at middle and center regions, whereas the microstructure at the center regions continues to demonstrate the coarse appearance. Deformation beyond this level ($\epsilon=24$ and $\epsilon=60$) results in evolution of an ultrafine microstructure throughout the disk characterized by rather equiaxed grains separated by HAGBs.

Fig 5.3 show the GB maps of strain reversal specimens at different strain level. The microstructure evolution for middle and edge region is similar for both the deformation modes, such that at lower strains the structure consist of huge LAGBs and with increasing strain gradually transforms into an ultrafine grained structure. However, at the center region in case of strain reversal specimens (Fig 5.3-(a-e)), the microstructure evolution is remarkably different compared to the monotonically deformation specimens. At the center after $\epsilon=12$, the microstructure starts to become ultrafine grained structure with high fraction of HAGBs, but beyond this deformation level (at $\epsilon=24$) the center region again shows presence of LAGBs and at $\epsilon=60$, the structure at center region remains essentially shows predominantly LAGBs network.

The evolution of structural parameters during HPT is shown in Fig 5.4 for both the deformation modes. It can be inferred from Fig 5.4 (a) that for monotonically deformed specimens, the average grain size decreases consistently throughout the disk with increasing strain. The average grain size at the edge reduces from $\sim 8\mu\text{m}$ after $\epsilon=1$ to 370nm after $\epsilon=60$. The average grain size at center, middle and the edge regions beyond strain level $\epsilon=24$ is nearly the same indicating a great homogeneity of microstructure. The fraction of HAGBs (Fig-5.4 (c)), in case of middle and the edge at strain level after $\epsilon=1$ increases from 8% and 14% respectively to 81% and 91% after $\epsilon=60$. In case of the center region the fraction of HAGBs first reduces up to the strain of $\epsilon=12$ and thereafter increases. The fraction of HAGBs at the edge remains almost unchanged beyond $\epsilon=12$.

During strain reversal deformation (Fig5.4-(b)) at $\epsilon=1$ the average grain size decreases from 31 μm to 4 μm in case of the edge region. At this strain the average grain size at the center also reduces to $\sim 27\mu\text{m}$. The average grain size at middle and edge region reduces continuously from 7 μm and 4 μm , respectively after $\epsilon =1$ to 410nm and 400nm at $\epsilon=24$. However at $\epsilon=60$, a slight increase in grain size to 470nm and 500nm, respectively at edge and middle is observed. At the center, the evolution of the grain size and fraction of HAGBs is noted to be quite unusual. The average grain size decreases up to strain of $\epsilon=12$ to $\sim 1\mu\text{m}$, and then significantly increases to $\sim 2.6 \mu\text{m}$ at $\epsilon=24$ and increases to further $\sim 5.7\mu\text{m}$ at $\epsilon=60$. This is consistent with the reappearance of LAGBs network already discussed before.

HAGBs fraction increases from 21% in case at edge region (Fig-5.4-(d)) after $\epsilon=1$ to 82% after $\epsilon=4$, thereafter no significant change could be observed as the HAGBs remains more or less constant up to $\epsilon=60$. In case of center region, the HAGBs first decrease after $\epsilon=4$ and then increase after $\epsilon=12$. At $\epsilon=24$ the fraction of HAGBs consistently reduces and at $\epsilon=60$ the fraction is only 15%.

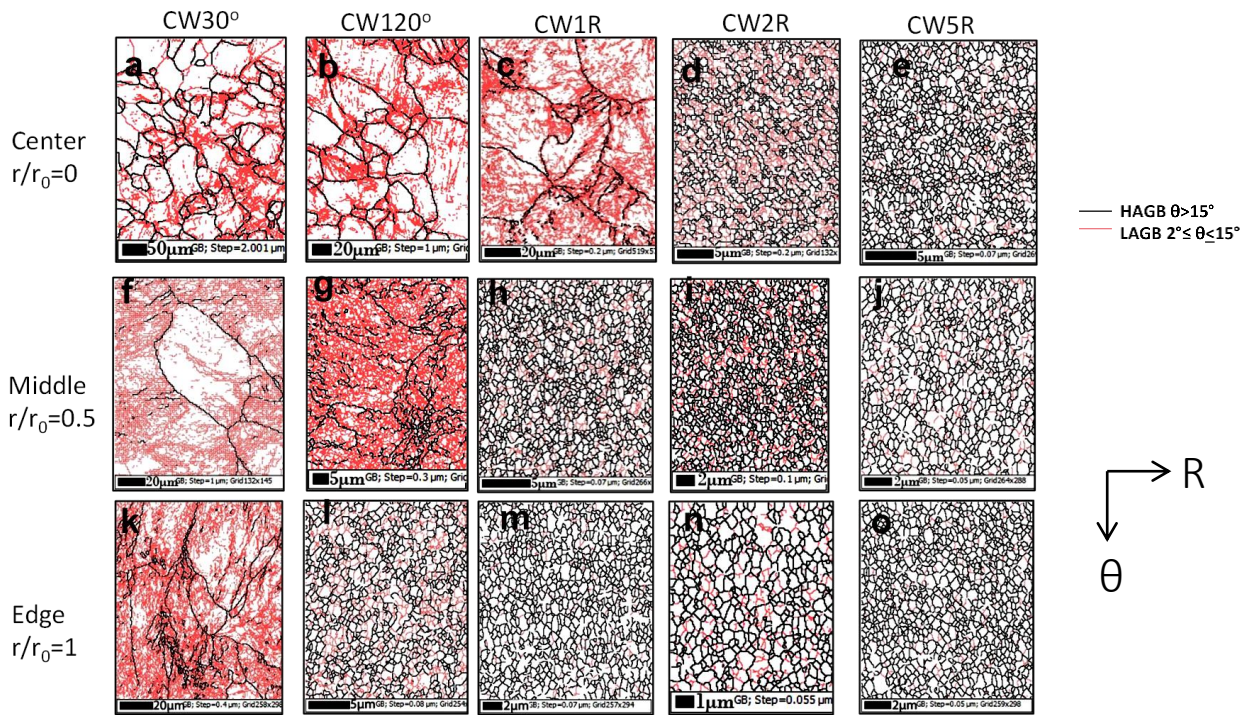


Fig. 5.2: Grain boundary maps of monotonically deformed Al-2.5Mg processed to different strain levels; center ($r/r_0=0$) (a-e), middle ($r/r_0=0.5$) (f-j) and edge regions ($r/r_0=1$) (k-o).

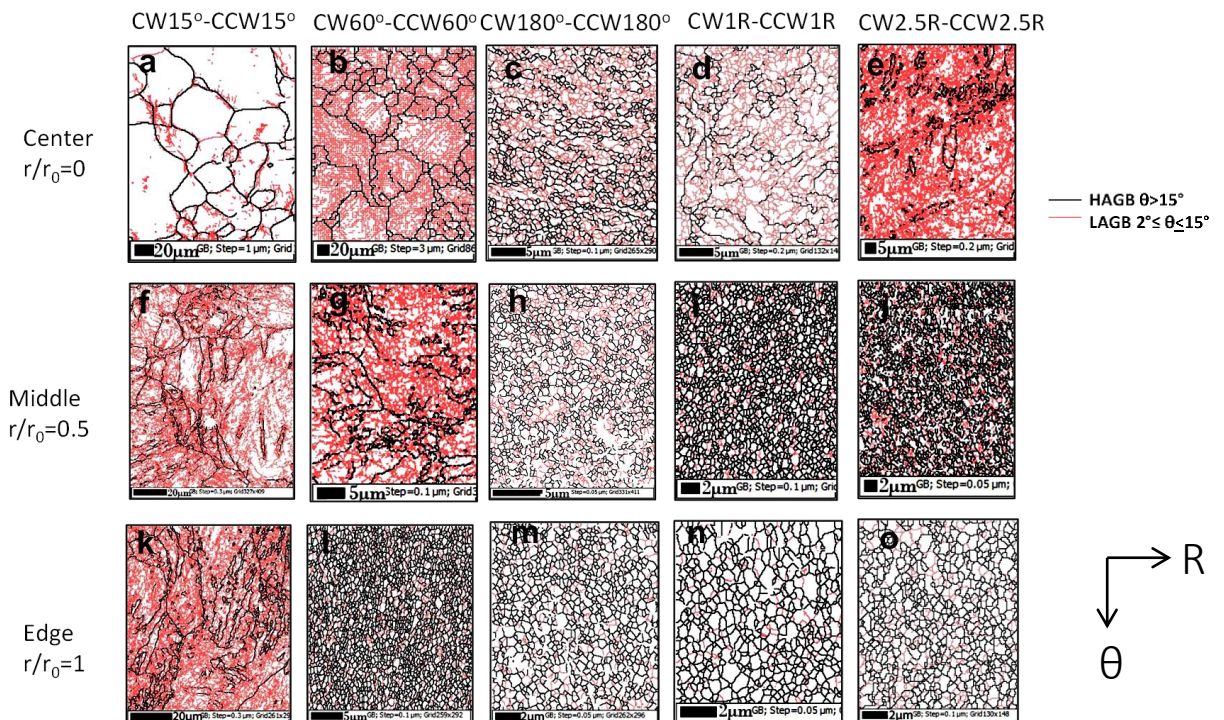
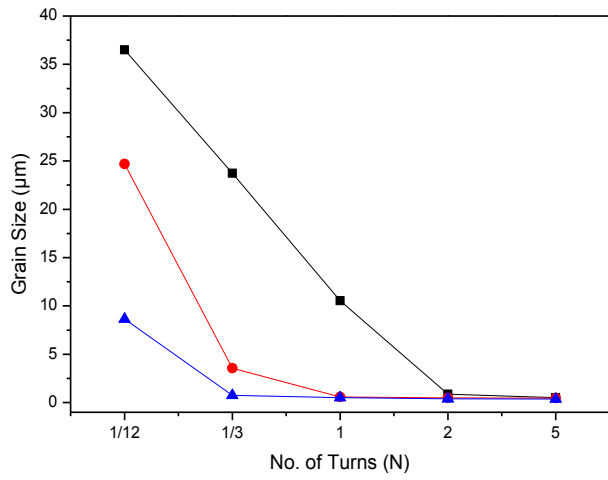
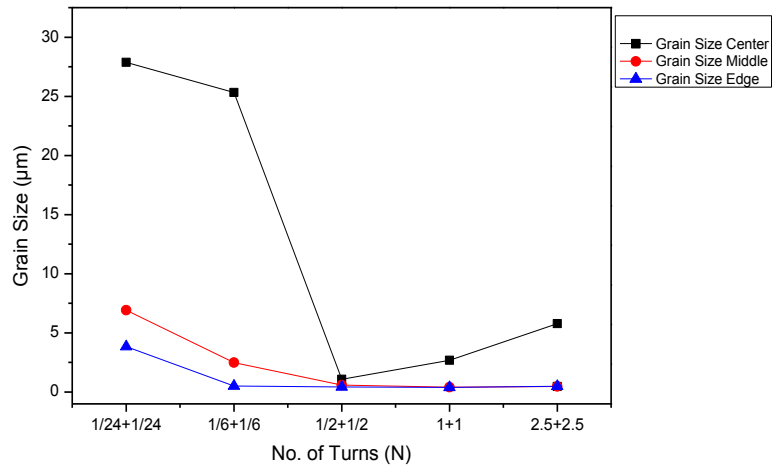


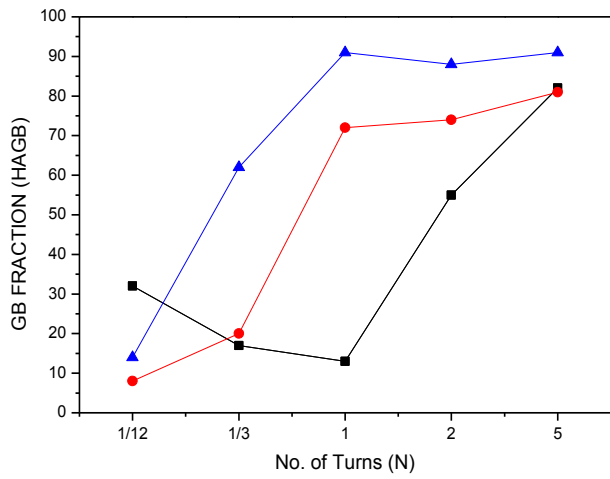
Fig. 5.3: Grain boundary maps of strain reversal deformed Al-2.5Mg processed to different strain levels; center ($r/r_0=0$) (a-e), middle ($r/r_0=0.5$) (f-j) and edge regions ($r/r_0=1$) (k-o).



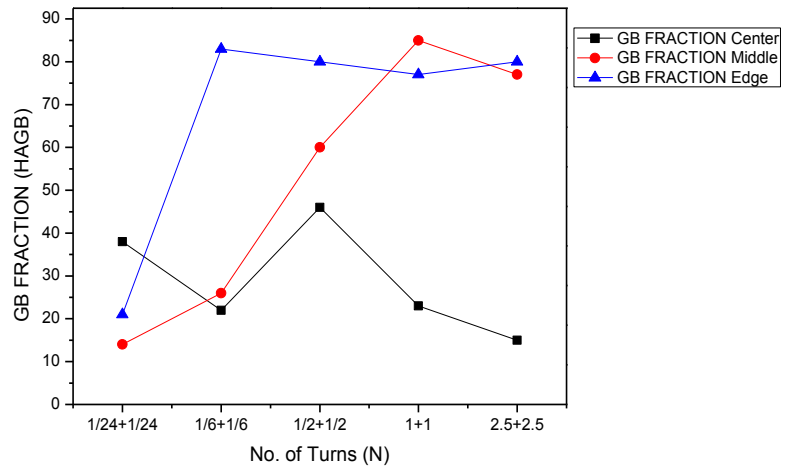
(a)



(b)



(c)



(d)

Fig 5.4: Variation of grain size ((a),(b)) and HAGB fraction ((c),(d)) with imposed strain in monotonous ((a),(c)) and strain reversal deformation ((b),(d)) modes.

5.2.2 Micro-texture Evolution

Figure 5.4 shows the (111) pole figure for monotonically (a-e) and strain reversal deformed (f-j) specimens. Figure 5.6 shows the $\Phi_2=45$ section of the ODF of monotonic ((a)-(e)) and strain reversal specimens ((f)-(j)). Fig. 5.7 shows the orientation maps depicting the spatial distribution maps of different texture components for monotonically ((a)-(e)) and strain reversal deformed specimens ((f)-(j)). Only the edge region has been considered here as maximum strain is obtained at the edge of the specimen as the torsional geometry. The ideal shear texture components are shown in (111) pole figure in Fig 5.4-(k) and listed in Table 1 [14]. Torsion texture development in F.C.C. metals are labelled $\{hkl\}\langle uvw \rangle$, where $\{hkl\}$ is a plane parallel to the shear plane and $\langle uvw \rangle$ is the shear direction Θ [15].

During monotonic deformation, at $\varepsilon = 1$ (Fig-5.5 (a), Fig 5.6(a)), noticeable presence of the C component can be observed having a volume fraction of $\sim 9\%$ (Fig.5.7(a)). Other components are present only in minor proportion and texture appears to be not very strong. The strength of the C component does not change much following straining to $\varepsilon=4$ (Fig.5.5(b), 5.6(b)) which is confirmed from the volume fraction of the C component ($\sim 8\%$) from the orientation map (Fig5.7(b)). However the volume fraction of A^*/A^{*-} component increases perceptibly ($\sim 6\%$). With further straining to at $\varepsilon=12$ (Fig.5.5(c), 5.6(c) and 5.7(c)) the C component increases to $\sim 11\%$ along with the A/A- component becomes noticeable $\sim 6\%$. The A^*/A^{*-} fraction remains almost unchanged. Following straining to $\varepsilon = 24$, the significant strengthening in the C ($\sim 14\%$) and A^*/A^{*-} ($\sim 12\%$) could be observed. The volume fraction of the A/A- remains almost unchanged. After an imposed strain of $\varepsilon=60$ both pole figure (Fig.5.5(e)) and ODF (Fig.5.6 (e)) reveal very weak intensities which clearly indicates extensive weakening of texture. This is further confirmed from the corresponding orientation map (Fig.5.7(e)) which shows considerable decrease in two major texture components, namely, C and A^*/A^{*-} as compared to the strain level $\varepsilon = 24$. The volume fraction of the C component is only 4% while that of the A^*/A^{*-} is $\sim 7\%$. The volume fraction of the A/A- ($\sim 6\%$) although does not show major change as compared to the $\varepsilon = 24$ deformed condition.

The texture evolution in the strain reversal deformed specimens show characteristic differences with the monotonically deformed specimens. During strain reversal deformation after an imposed strain of $\epsilon=1$ (Fig-5.4 (f), 5.6(f) and 5.7(f)), the texture appears quite weak such that the volume fraction of the A^*/A^{*-} component is only 4%. Other components are present even in minor proportions while the volume fraction of the C component is $\sim 2\%$. All the components are strengthened after an imposed strain of $\epsilon=4$ (Fig.5.5(g), 5.6(g) and 5.7(g)). The A^*/A^{*-} component appears relatively stronger having a volume fraction of $\sim 15\%$ while the volume fraction of A/A^- is found to be $\sim 9\%$. The fraction of the C component is almost negligible. At $\epsilon=12$ (Fig.5.5(h), 5.6(h) and 5.7(h)) remarkable change in texture could be observed such that the volume fraction of the two major components A^*/A^{*-} and A/A^- decreases to $\sim 6\%$ and 4% , respectively. Beyond this strain level volume fraction of all but the C component increases drastically while the volume fraction of other components show only marginal changes. A strong C component having a volume fraction $\sim 18\%$ is observed at the highest strain level of $\epsilon=60$ (Fig.5.5(k), 5.6(k) and 5.7(k)). The volume fraction of the A^*/A^{*-} , A/A^- and B/B^- are found to be very similar amongst them lying between 5-7% and much lower than the volume fraction of the C component.

The texture evolution in Al-Mg subjected to the two different processing routes is summarized in Figures 5.8(a) and 5.8(b) for monotonically and strain reversal deformed specimens.

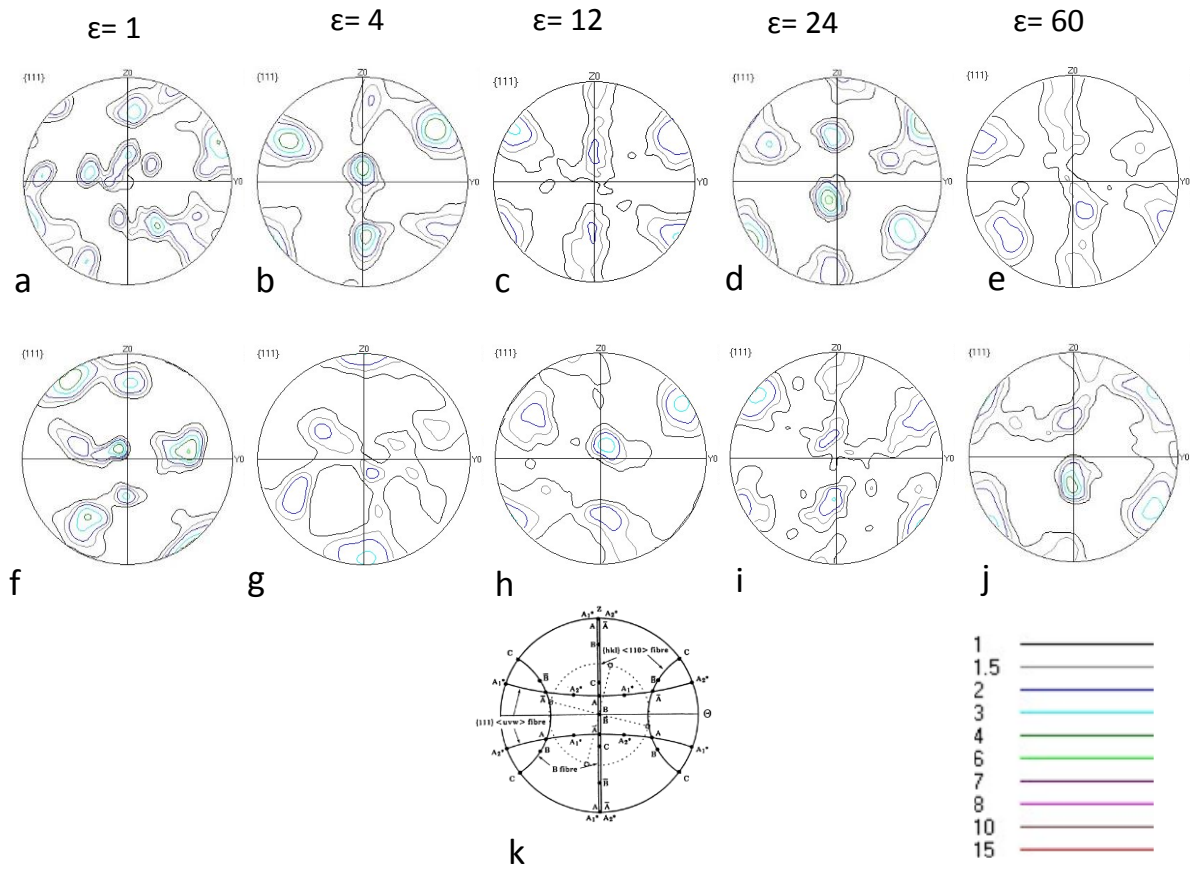


Fig 5.5: (111) pole figure of the edge regions of monotonically (a-e) and strain reversal (f-j) specimens. The ideal texture components in (111) pole figure is shown in (k) [20].

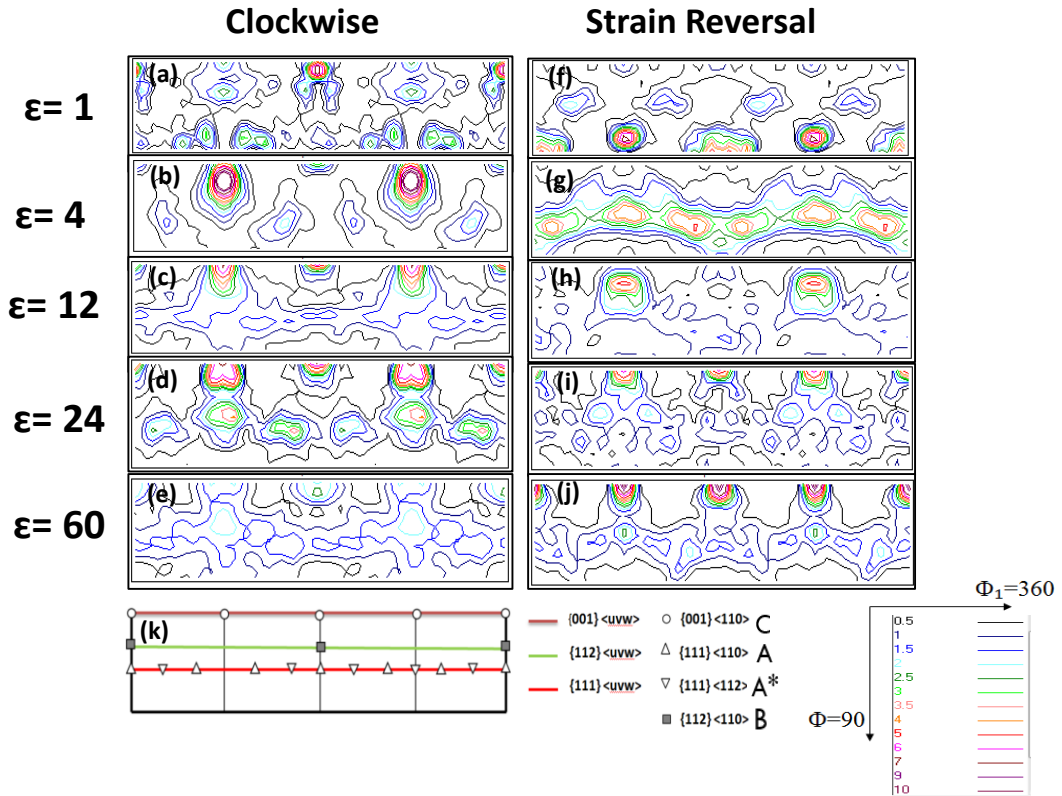


Fig 5.6: $\Phi_2=45^\circ$ sections of the ODFs of monotonically (a-e) and strain reversal (f-j) deformed obtained from the edge region ($r/r_0=1$). The ideal positions of ideal shear texture components is shown in (k) [21].

Table 1: Ideal texture components for fcc metals

Component	$\{hkl\}\langle uvw \rangle$
A	$\{1\bar{1}\bar{1}\}\langle 110 \rangle$
A-	$\{\bar{1}11\}\langle \bar{1}\bar{1}0 \rangle$
A*	$\{\bar{1}\bar{1}1\}\langle 112 \rangle$
A*-	$\{11\bar{1}\}\langle 112 \rangle$
B	$\{\bar{1}\bar{1}2\}\langle 110 \rangle$
B-	$\{1\bar{1}\bar{2}\}\langle \bar{1}\bar{1}0 \rangle$
C	$\{001\}\langle 110 \rangle$

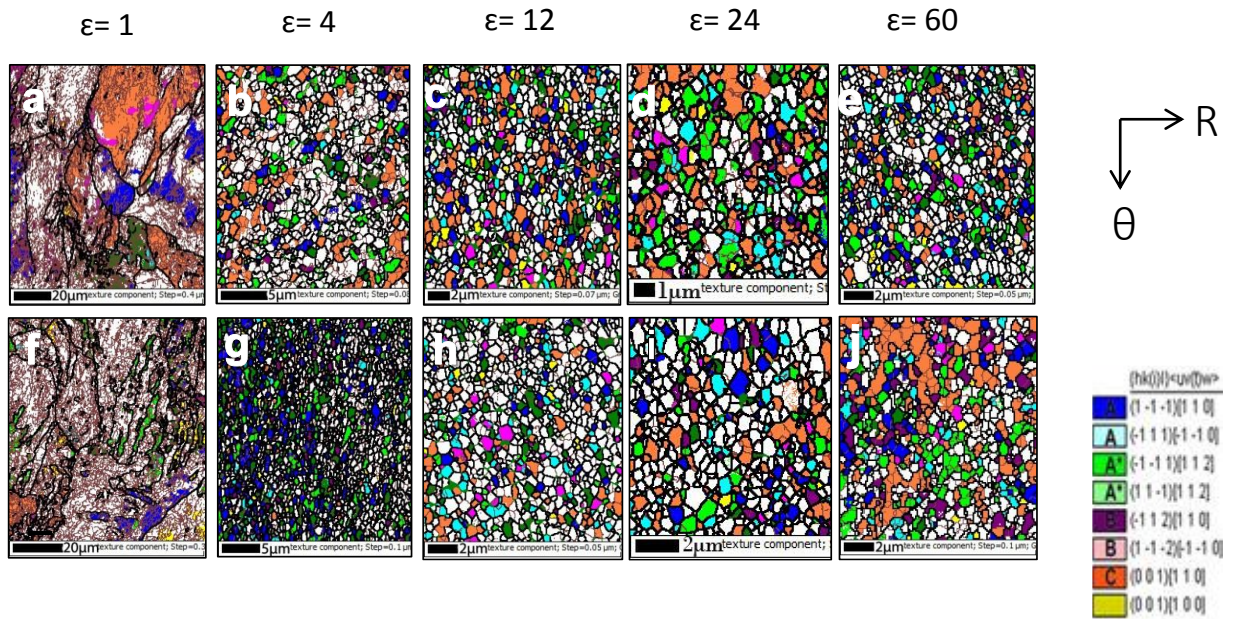


Fig 5.7: EBSD maps of monotonically (a-e) and strain reversal deformed specimens (f-j).

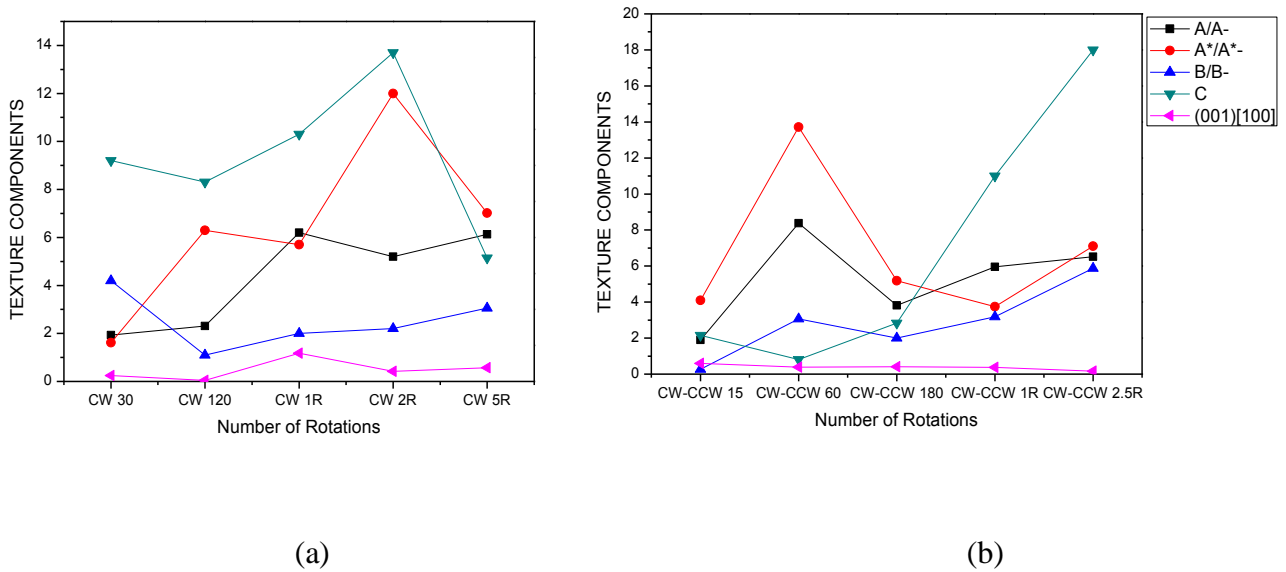


Fig 5.8: Variation of texture component with imposed strain for (a) monotonically and (b) strain reversal deformed specimens.

5.2.3 Microhardness Properties

The distribution of hardness values across the diameters are shown in Fig-5.9 for the disks processed by HPT through monotonic (CW) and strain reversal (CW-CCW)

deformation modes. The lower straight line shows hardness value of Hv=62 of the annealed starting material used for the HPT processing.

The characteristic hardness distribution of HPT processed disks with minimum in the center and maximum at the edges can be easily seen at all strain levels. The hardness values of the monotonically and strain reversal deformed specimens at the same strain level are found to be very similar and shows very similar distribution characterized by higher hardness values at the edge and minimum at the center which is typical for HPT processed disks. However, the major difference between the hardness distribution of the two processing routes is apparent at the highest strain level i.e. at $\epsilon=60$. At this strain level the hardness at the edge regions of the monotonically and strain reversal deformed specimens are found to be very similar ~128 and 125 respectively. On the other hand at the center region the hardness values are found to be different ~107 and 87, respectively clearly indicating the hardness at the center of strain reversal deformed specimen is much lower than edges regions and also significantly lower compared to the center regions of its monotonically deformed counterpart. It is clearly noted that hardness homogeneity is not achieved in any of the processing routes even after the imposition of such huge strain.

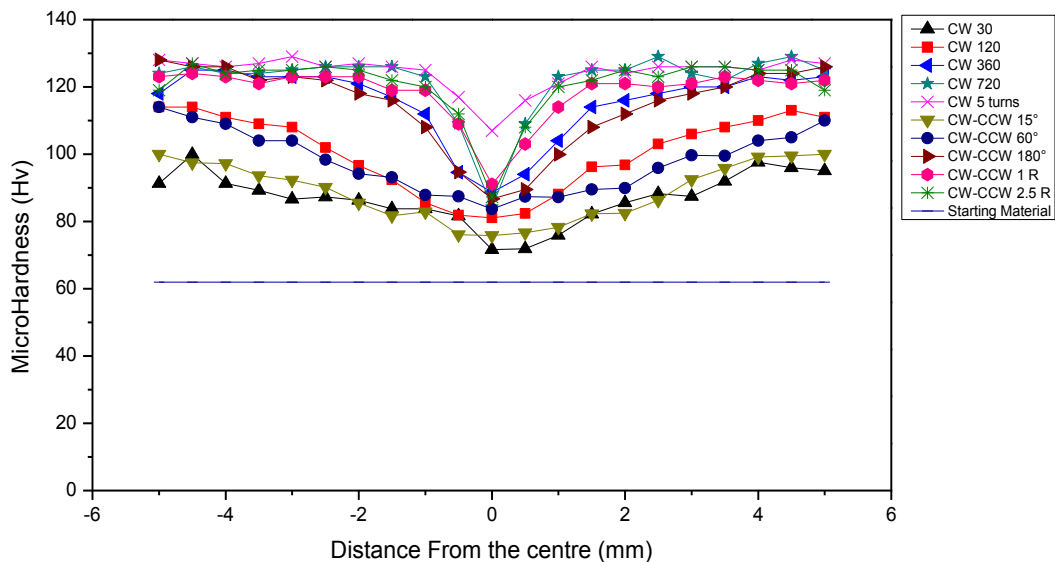


Fig 5.9: Hardness distribution in monotonically and strain reversal deformed specimens at different strain.

Chapter 6

Discussion

6.1 Evolution of microstructure and hardness properties

The process for the formation of grain refinement has been explained on the basis of subdivision behavior [22-25]. The theory suggests that the microstructural refinement takes place by dislocation generation (when the strain is applied) followed by evolution of cell or substructure made up of dislocation cell walls having low misorientation. With the continued deformation dislocation starts accumulating at the cell boundaries resulting in increasing misorientation of the boundaries and decrease in cell size. Finally the low angle dislocation boundaries transform to high angle boundaries resulting in the formation of ultrafine microstructure (Fig.6.1). This process of grain refinement might be helpful to discuss the grain refinement process during monotonic and strain reversal deformation of the two aluminium alloys in the present study.

In the two different aluminium alloys deformed by the two different deformation modes, the evolution of the ultrafine structure follows similar trend. The starting microstructure composed of large recrystallized grains throughout the disk develops prominent LAGBs network inside the grains and with increasing strain the structure is continuously refined such that ultimately at higher strains ultrafine microstructure characterized by equiaxed grains separated by HAGBs evolve throughout the disk. The grain refinement of the alloys start from the edge region and gradually extends towards the center with increasing strain for both the deformation modes (Fig 4.2, Fig 4.3, Fig 5.2, and Fig 5.3). The only exception to this is in case of Al-2.5Mg at the center regions during strain reversal deformation as already indicated (Fig 5.3 (a)-(e)). Thus the microstructural evolution of the HPT processed disks are in agreement with the mechanism outlined in the grain subdivision process which may

thus be considered to be primary mechanism for the evolution of ultrafine structure in the two aluminium alloys.

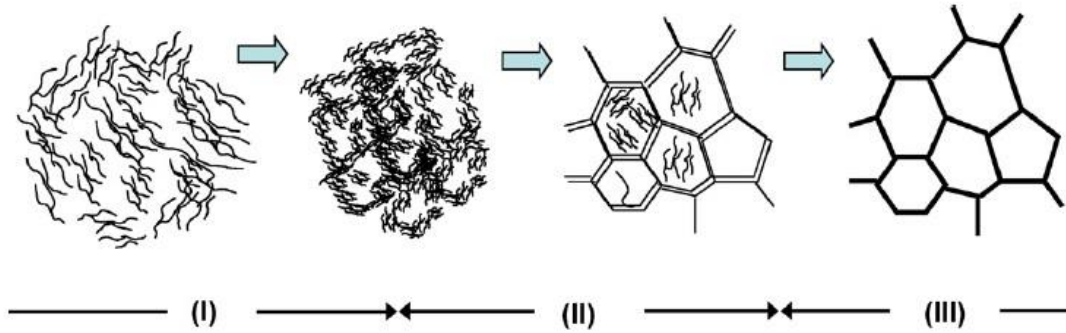


Fig 6.1: Schematic illustration of microstructural evolution with low strain to high strain in regions I-III. The double line in region II represent LAGBs and thick lines in region III represent HAGBs. [26]

In order to understand the differences in the microstructural evolution in two aluminium alloys deformed by the two different deformation modes the edge regions are compared as the maximum strain is achieved here as per the torsional geometry. The variation of grain size and fraction of HAGBs near the edge regions ($r/r_0 \sim 1$) with imposed strain are represented in Fig. 6.2 ((a)-(b)) for monotonically and strain reversal deformed specimens.

It can be clearly seen for both the deformation modes the grain size decreases with the increasing strain. It is observed that for both the alloys processed by the two deformation modes significant grain refinement happens after $\epsilon=4$ (CW 120° and CW(60°)-CCW(60°)). Beyond this only slight decrease in the grain size could be observed. It may be noted that in the monotonic deformation mode, the average grain size of Al-2.5Mg and 2N-Al decrease drastically after $\epsilon=4$ (CW 120°) to 760 nm and 1.7 μm respectively. Thereafter the grain size further reduces to ~ 370 nm and 900nm after $\epsilon=60$ (CW 5R) (Fig. 6.2(a)). However minor fluctuation in the grain size reduction in 2N-Al is observed as compared to Al-2.5Mg which shows very consistent behavior. In strain reversal deformation the grain refinement in Al-2.5Mg and 2N-Al

occurs after $\epsilon=4$ (CW(60°)-CCW(60°)) and average grain size achieved is $\sim 500\text{nm}$ and $1.5\ \mu\text{m}$ (Fig 6.2 (a)). The grain size reduces slightly in both the cases and the final grain size achieved after $\epsilon=60$ (CW(2.5R)-CCW(2.5R)) in Al-2.5Mg and 2N-Al is $\sim 500\text{nm}$ and $\sim 900\text{nm}$ respectively. Thus, it may be clearly seen that strain reversal affect the grain size in the two materials at lower strain regime, however, at large strain levels no appreciable variation could be evidenced.

In monotonically deformed Al-2.5Mg, the fraction of HAGB increases consistently till $\epsilon=12$ (CW 1R) and thereafter remains nearly unchanged (Fig. 6(b)). In 2N-Al, the fraction of HAGB first increases at $\epsilon=4$ (CW120°) and then decreases at $\epsilon=12$ (CW 1R). This is in accordance with the grain size reduction, where the grain size is lower at $\epsilon=4$ (CW 120°) and then increases at $\epsilon=12$ (CW 1R). At $\epsilon=60$ (CW 5R), the fraction of HAGBs for both the alloys is similar $\sim 90\%$. At strain reversal deformation, the fraction of HAGBs increases consistently and at $\epsilon=60$ (CW (2.5R)-CCW(2.5R)) the fraction is similar for both the cases $\sim 80\%$. However, it is clearly observed that irrespective of the alloy system strain reversal results in lower HAGB fraction.

The retardation in the formation of HAGBs in strain reversals has also been reported by Hasegawa et al. [27]. It has been argued that due to reversal straining the cell walls and sub boundaries which were developed by pre straining became unstable. It is also reported that at early strains, the dislocation density reduced by $\sim 16\%$ due to strain reversals. In conclusion, the dissolution of cell walls due to strain reversal was related to Bauschinger Effect. The effect of strain reversal during HPT has also been studied by Orlov et al [17]. It is reported that there is no contribution of the effect of strain reversal on grain size, but significant retardation in the formation of HAGBs was observed. The authors have suggested the mechanism of this is related to Bauschinger Effect, which works not only in near elastic deformation but also for far plastic deformation. The present results are in thus good agreement with the results reported by Orlov et al [17].

The hardness distribution plots of 2N-Al (Fig 4.9) reveal excellent homogeneity at higher strains whereas that of Al-2.5Mg (Fig 5.9) reveal homogeneity at the edge regions only. However smaller grain size combined with high hardness is achieved in Al-2.5Mg for both the deformation modes as compared to 2N-Al. This is clearly attributed to the solid-solution strengthening effect of Mg alloying and the fact that addition of Mg in Al influences the dislocation density and strength. Addition of Mg causes solid solution strengthening and hindrance to dislocation movement (by pinning the dislocations) resulting in hindrance in annihilation of dislocations during deformation which ultimately increases the dislocation density [28]. The hardness values obtained for Al-2.5Mg agrees with those of Horita et al [29], who reported that the reverse straining in HPT of Al-Mg-Sc did not contribute to increase in hardness, rather decreased hardness is observed in strain reversal specimens as compared to monotonically deformed specimens. Higher hardness values are observed in 2N-Al deformed by strain reversal. It has been reported by Kawasaki et al. [30] that slight higher hardness is observed in high purity Al when deformed by cyclic-HPT(c-HPT). The authors justified this by a simple theory: during strain reversal, the dislocations formed during initial monotonic direction, flow back from the dislocation pile ups resulting in slightly less total strain as compared to its counterpart. In the present results, in 2N-Al, higher hardness is observed but the grain size obtained by the two deformation modes remains similar.

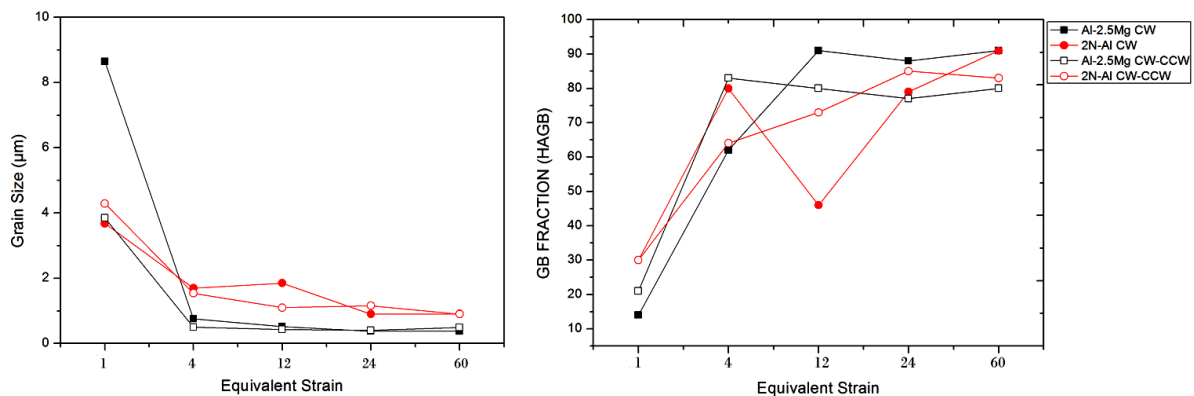


Fig. 6.2: Variation of (a) grain size (b) fraction of HAGBs with the imposed strain for monotonically and strain reversal deformed specimens.

6.2 Evolution of Texture

Torsion texture evolution in Al and Cu has been studied by Montheillet et al [15]. The report discussed development of torsion texture during conventional deformation. The results from the pole figure of Cu and Al show similarity with each other. During low strains in Cu, the A and A* component was observed which was replaced by the C component as the strain increases. The A*- part was also observed at higher strains. The strength of the B component increases with the increasing strain. Similar results are observed in case of Al (Fig 6.3 (a)-(d)), where the A component is present in low strains and is gradually replaced by the C component at higher strains.

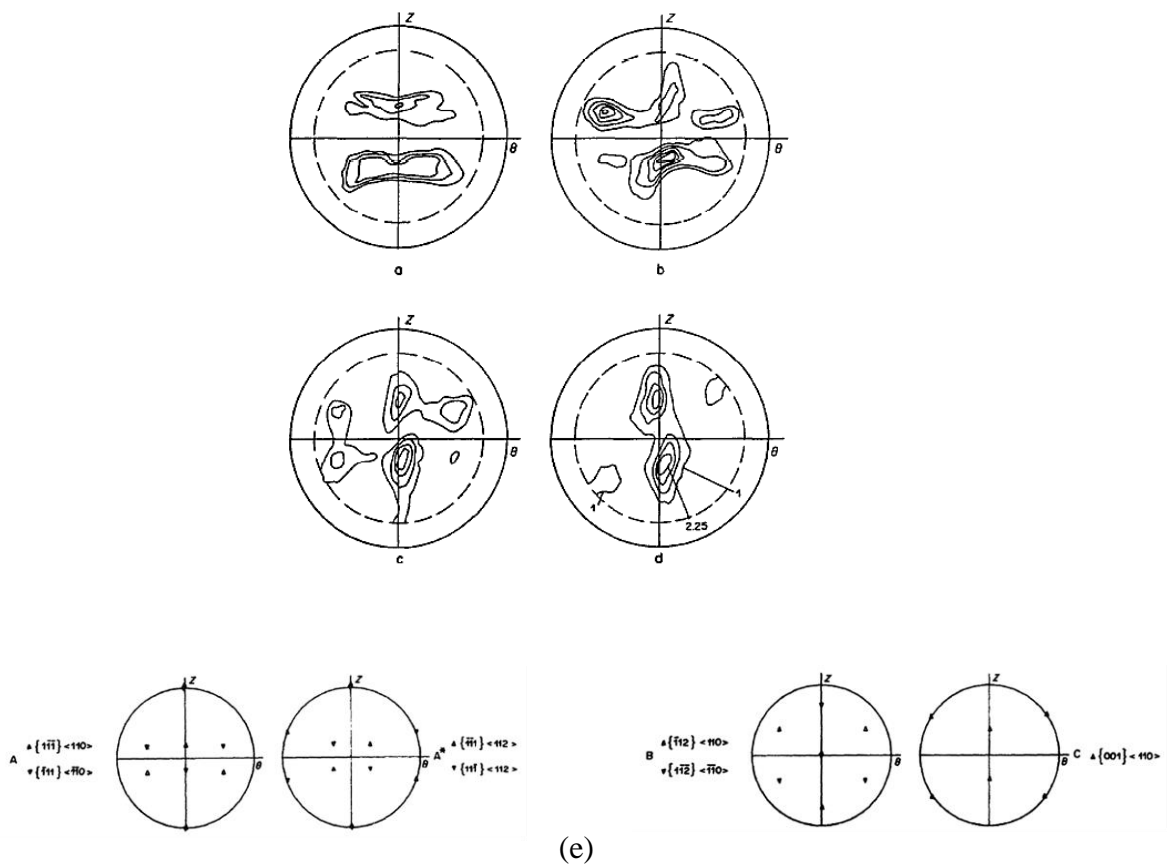


Fig.6.3: Torsion texture of Aluminum at 20°C and $7 \times 10^{-3} \text{ s}^{-1}$; (111) pole figures, (a) initial state, (b) $\epsilon=0.62$, (c) $\epsilon=2.18$, (d) $\epsilon=4.98$, (e) Ideal texture components in (111) pole figure. [15]

The texture evolution in aluminum alloys processed by the two deformation modes shows the presence of same ideal shear components A/A^* , A^*/A^{*-} , B/B^* and C which are also observed during conventional torsional deformation (Fig.6.4).

In 2N-Al (Fig.6.4 (a)-(d)), the A/A^* component follows the similar trend in both the deformation modes. The component can be seen to increase till $\epsilon=12$ (CW 1R) and then decreases after $\epsilon=24$ (CW 2R) in both the deformation modes. The A/A^* component has similar fraction at $\epsilon=60$ (CW 5R). The A^*/A^{*-} component follows a completely opposite trend for both the deformation modes. The fraction of A^*/A^{*-} component is lower in monotonic deformation at $\epsilon=1$ (CW30°) as compared to its strain reversal counterpart. The fraction increases till $\epsilon=12$ (CW 1R) and thereafter decreases at $\epsilon=24$ (CW2R) and increased again at $\epsilon=60$ (CW5R). Exactly opposite trend can be seen for strain reversal mode, where the A/A^* component decreases after $\epsilon=12$ (CW(180°)-CCW(180°)), increases after $\epsilon=24$ (CW(1R)-CCW(1R)) and ultimately decreases after $\epsilon=60$ (CW(2.5R)-CCW(2.5R)). The fraction of the B/B^* component is less in monotonic deformation as compared to strain reversal at lower strain. With the increase in strain the fraction increases consistently in monotonic deformation however in strain reversal mode opposite trend is observed, where at lower strain the fraction is very high and then consistently decreases with increasing strain. The C component increases after $\epsilon=4$ (CW 120°) in both the deformation mode but relatively sharp increase is observed in monotonic deformation. The fraction reduces sharply in monotonic deformation at $\epsilon=12$ (CW 1R), whereas for strain reversal it increases significantly. The fraction then is observed to increase in monotonic deformation whereas it decreases in strain reversal one. The fraction is observed to be similar in both the deformation modes at $\epsilon=60$ (CW 5R and CW2.5R-CCW2.5R).

In Al-2.5Mg (Fig.6.4 (a)-(d)), the A/A^* fraction increases with increasing strain in both the deformation modes and at higher strain ($\epsilon=60$ (CW5R and CW(2.5R)-CCW(2.5R)) the values are quite similar. The only exception is at $\epsilon=4$ (CW120° and CW(60°)-CCW(60°)), where the fraction decreases in strain reversal deformation and increases in monotonic deformation. The A^*/A^{*-} component follows similar trend for both the deformation modes and the fraction is similar at highest

strain value with the exception of $\varepsilon=24$ (CW2R and CW(1R)-CCW(1R)), where the fraction increases in monotonic deformation and decrease in strain reversal mode. The B/B⁻ component increases consistently for both the deformation modes and at $\varepsilon=60$ (CW5R and CW(2.5R)-CCW(2.5R)) the fraction is higher in strain reversal as compared to monotonic deformation. The C component also follows similar trend in both the deformation modes with the exception of $\varepsilon=24$ (CW2R and CW(1R)-CCW(1R)) where the fraction decreases in monotonically deformed specimen but increases in the strain reversal deformed specimen.

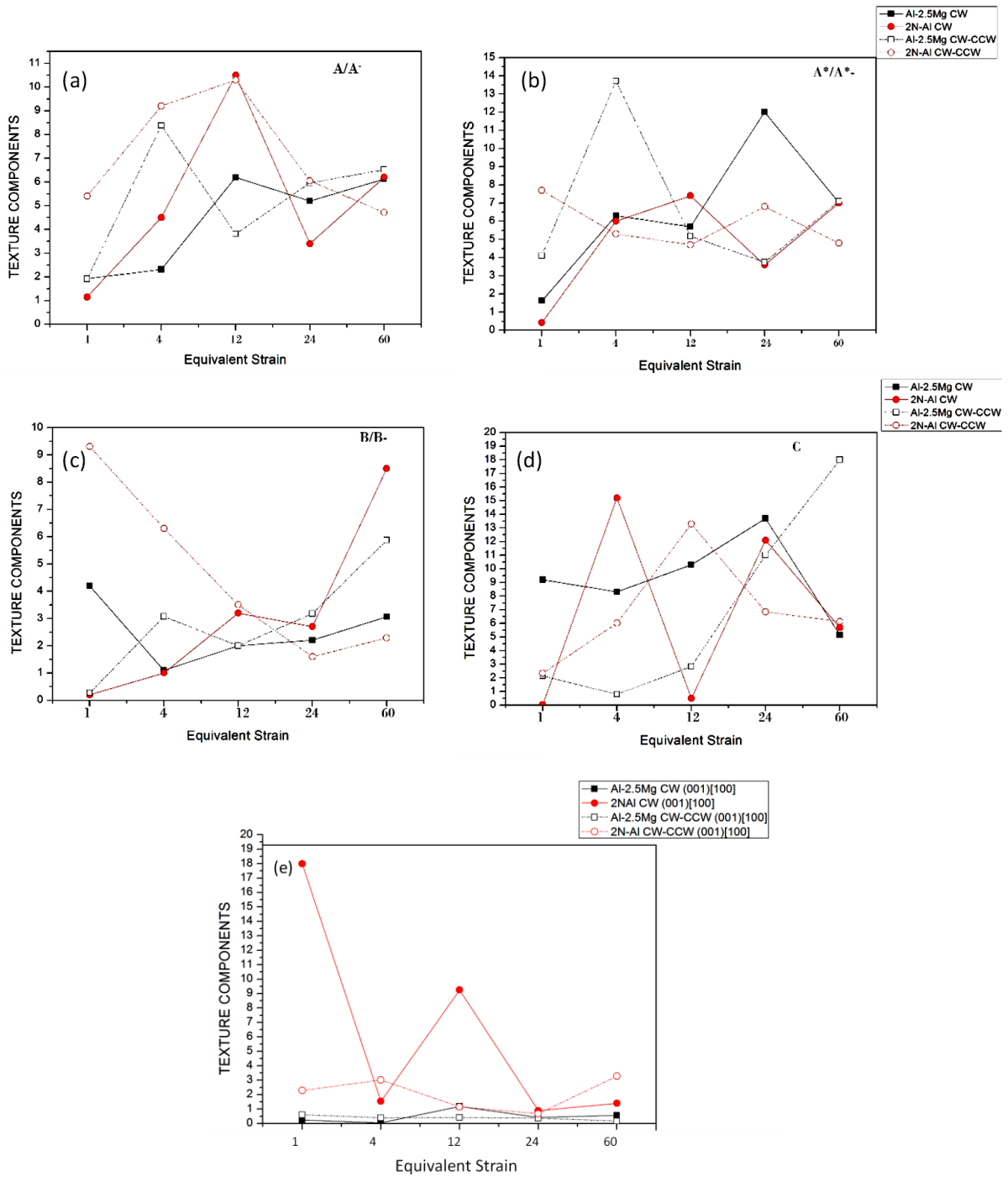


Fig.6.4: Volume fractions of the texture components with imposed strain for monotonically and strain reversal deformed two alloys: (a) A/A⁻ component; (b) A*/A*⁻ component; (c) B/B⁻ component (d) C component; (e) (001)[100] component.

It may be also helpful to relook the volume fraction of different texture components separately for each deformation mode (Fig.6.5 and Fig.6.6). In monotonically deformed 2N-Al and Al-2.5Mg specimens (Fig.6.5 (a)-(c)), increase in the volume fraction of the C and B/B⁻ component is observed. Presence of A*/A*⁻ is also observed in the present results. The observations are in agreement of the results reported by Montheillet et al [15] and Toth et al [20]. The work carried by Orlov et al [9, 31] although up to a much smaller strain level agrees with the present results. A rise in the C component observed in 2N-Al from $\epsilon=1$ (CW30°) to $\epsilon=4$ (CW120°) may be considered not vastly different from the strain regime in the study reported by Orlov et al [9]. Very similar behavior can be seen in Al-2.5Mg, where the C component is strengthened to strain level of $\epsilon=24$ (CW 2R). It is interesting to note that at this strain level the strength of the C component increases at the expense of A/A⁻ component. In the present case, at the highest strain i.e. at $\epsilon=60$ (CW 5R) in Al-2.5Mg, the fraction of the C, A*/A*⁻ and B/B⁻ components decreases and the texture appears to be weakened which is in well accordance with the study reported by Orlov et al [9] and Aicha et al [21], where it has been reported that at higher strains the texture becomes weak and randomized. On the other hand, reports on texture evolution during strain reversal deformation in HPT is rather limited [9]. It has been reported during strain reversal deformation for pure (99.99%) Al, that at lower strains the A/A⁻ and A*/A*⁻ components dominate. The (001)[100] component increases after $\epsilon=1$ and at highest strain, significance presence of the (001)[100] was observed. Similar results is observed in present report in 2N-Al (Fig. 6.6(d)) that the fraction (001)[100] component increases after $\epsilon=4$ (CW(60°)-CCW(60°)). At $\epsilon=60$ (CW(2.5R)-CCW(2.5R)), considerable presence of (001)[100] is observed in 2N-Al. However, in Al-2.5Mg, the (001)[100] component is found in negligible fraction. But significant presence of A/A⁻ and A*/A*⁻ can be observed in Al-2.5Mg (Fig.6.6(a)-(b)) at lower strains which is in agreement with the reported results [13]. At higher strains the C component (Fig. 6.6 (c)) can be seen to increase in both the alloys with exceptionally high fraction in case of Al-2.5Mg alloy.

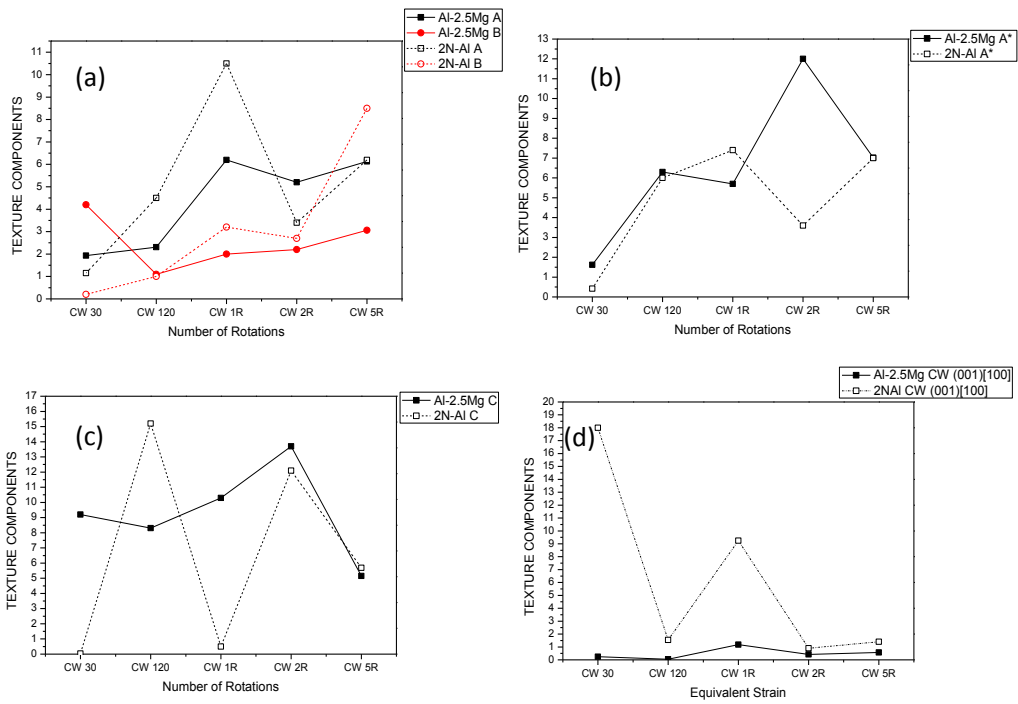


Fig.6.5: Volume fractions of the texture components with imposed strain for monotonically deformed two alloys: (a) A/A- and B/B- components; (b) A*/A*- components; (c) C component; (d) (001)[100] component.

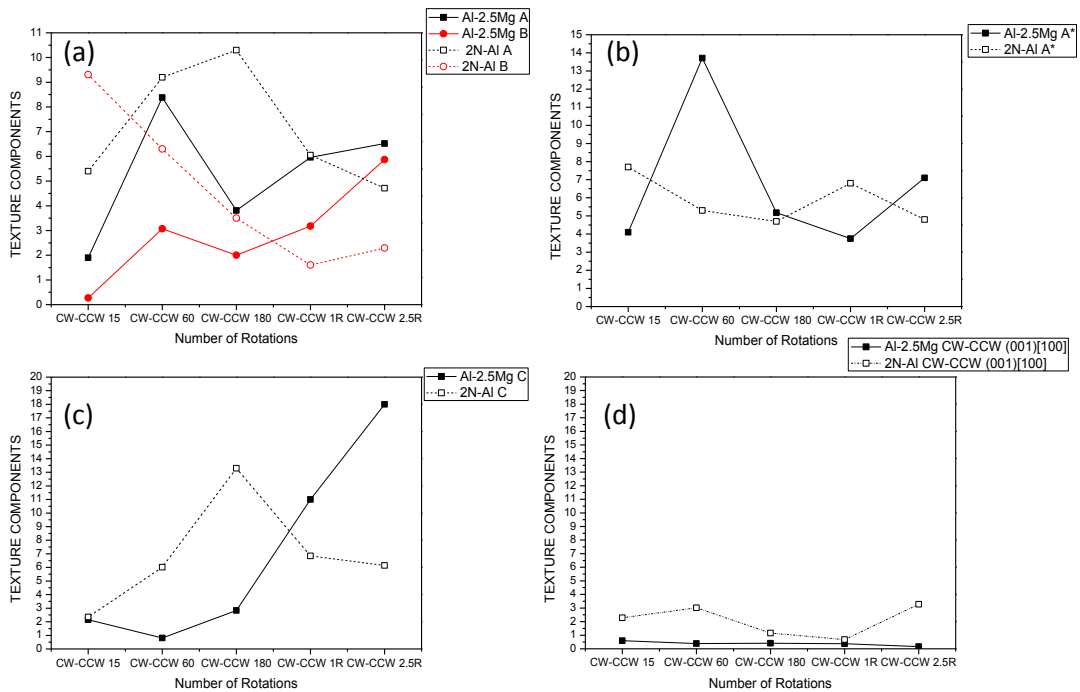


Fig.6.6: Volume fractions of the texture components with imposed strain for strain reversal deformed two alloys: (a) A/A- and B/B- components; (b) A*/A*- components; (c) C component; (d) (001)[100] component.

In the study reported by Gilormini et al [32], with the increase in the number of rotations, the periodic rise and fall of A/A^- , A^*/A^{*-} and C is observed. The reason for this might be due to successive lattice rotations of the A_1^* into A_2^* , A_2^* into C, and then C into A_1^* . The variations in the texture components is observed but such cyclic variations at some strain values (at $\epsilon = 12$ (CW 1R) for Al-2.5Mg and at $\epsilon = 24$ (CW 2R) for 2N-Al where A^*/A^{*-} can be seen to decrease and the C component increases) agree with the experimental results. At the highest strain ($\epsilon = 60$ (CW 5R)), the volume fraction of the shear components in monotonically deformed alloys is found to decrease and texture becomes weak in Al-2.5Mg and randomized in 2N-Al. This weakening of texture may be due to extreme grain refinement in which the grain rotation may lead to texture weakening. This is also observed in a study by Zhilyaev et al.[33] where HPT results in better grain refinement as compared to ECAP, but stronger texture was observed in ECAP and weaker after HPT processing.

The evolution of A/A^- and C components in 2N-Al and Al-2.5Mg deformed by the two different routes follows similar trend. The B/B^- component in Al-2.5Mg alloy follows similar trend in both the deformation modes. However in 2N-Al the A^*/A^{*-} and B/B^- component show reverse trends. It may be observed that the strain reversal affects the texture evolution in both the aluminum alloys.

Chapter 7

Summary and Conclusion

The effect of strain reversal during high pressure torsion on the evolution of microstructure, texture and hardness properties of two aluminum alloys, namely, high purity aluminum (2N-Al) and Al-2.5%Mg has been studied. The microstructure, microtexture and hardness have been characterized by using EBSD and Vickers hardness testing. The following conclusions are drawn from the present study:

1. The microstructural evolution reveals that the grain refinement for the two deformation modes for the two alloys follows similar trend i.e. initial recrystallized microstructure with large grain size throughout the disk develop prominent LAGBs network inside the grains and ultimately at higher strains ultrafine equiaxed grains separated by HAGBs throughout the disk evolve. The final grain size of 2N-Al and Al-2.5Mg deformed by both the deformation modes at higher strain level is observed to be similar. However strain reversal effect the grain size at lower strain regime in two materials.
2. The fraction of HAGBs increases with the imposed strain for the two alloys in both deformation modes. However the fraction of HAGBs for monotonically deformed specimens is found to be higher than strain reversal deformed alloys.
3. The hardness distribution of 2N-Al reveals excellent homogeneity at higher strains whereas for Al-2.5Mg hardness homogeneity is not achieved and is limited to edge regions only at higher strains. Slightly higher hardness is observed for 2N-Al subjected to strain reversals at higher strains. The hardness of Al-2.5Mg at center region subjected to strain reversal at high strain regime is observed to be strikingly less as compared to its monotonically deformed counterparts.

4. The evolution of A/A^- and C components in 2N-Al deformed by the two deformation modes follows similar trend. The A^*/A^*- and B/B^- component shows reverse trend. The (001)[100] component is observed at lower strains and a mixed texture is observed during monotonic deformation. In strain reversal, a mixed texture but relatively stronger B/B^- component is observed at lower strains whereas weak texture is observed at higher strains.
5. In Al-2.5Mg, similar trend is observed for A/A^- , C and B/B^- component for both the deformation modes. A strong C component is observed at lower strains and a mixed texture is observed at higher strains for monotonically deformed specimens. During strain reversals, a weak texture is observed at the lower strains and with the increase in the imposed strain, the C component gradually becomes stronger.

References

- [1] T. Shanmugasundaram, M.Heilmaier, B.S.Murty, V.Subramanya Sarma, *On the Hall-Petch relationship in a nanostructured al-Cu alloy*. Materials Science and Engineering A, 2010. **527**: p. 7821-7825
- [2] Erb U, El-Sherik AM, Palumbo G, Aust KT, *Synthesis, structure and properties of electroplated nanocrystalline materials*. Nanostructured Materials, 1993. **2**: p. 383-390.
- [3] Gleiter H. In: Hansen N, Horsewell A, Leffers T, Lilholt H, editors, *Deformation of polycrystals: Mechanisms and microstructures*. Roskilde, Denmark: Riso National Laboratory, 1981: p. 15
- [4] Koch CC, Cho YS., *Nanocrystals by high energy ball milling*. Nanostruct Mater, 1992. **2**: p. 207-212
- [5] R.Z. Valiev, R.K. Islamgaliev, I.V. Alexandrov, *Bulk nanostructured materials from severe plastic deformation*. Progress in Materials Science, 2000. **45(2)**: p. 103-189
- [6] Y. Saito, H. Utsunomiya, N.Tsuji, T.Sakai, *Novel ultra-high straining process for bulk materials—development of the accumulative roll-bonding (ARB) process*. Acta materialia, 1999. **47(2)**: p. 579-583
- [7] AP. Zhilyaev, T.G. Langdon, *Using high-pressure torsion for metal processing*. Fundamentals and applications Progress in Materials Science, 2008. **53(6)**: p. 893-979
- [8] P.P.Bhattacharjee, M.Joshi, V.P.Chaudary, M.Zaid, *The effect of starting grain size on the evolution of microstructure and texture in nickel during processing by cross-rolling*. Materials Characterization, 2013. **76**: p. 21-27
- [9] D. Orlov, Pinaki Prasad Bhattacharjee, Yoshikazu Todaka, Minoru Umemoto, Nobuhiro Tsuji, *Texture evolution in pure aluminum subjected to monotonous and reversal straining in high-pressure torsion*. Scripta Materialia, 2009. **60 (10)**: p 893-896
- [10] M.Kawasaki, Saleh N. Alhejeri, Cheng Xu, Terence G. Langdon, *The development of hardness homogeneity in pure aluminum and aluminum alloy disks processed by high-pressure torsion*. Materials Science and Engineering A, 2011. **529**: p. 345-351
- [11] Cheng Xu, Zenji Horita, Terence G. Langdon, *The evolution of homogeneity in an aluminum alloy processed using high-pressure torsion*. Acta Materialia, 2008. **56 (10)**: p. 5168-5176

- [12] M. Kawasaki, Roberto B. Figueiredo, Terence G. Langdon, *Twenty-five years of severe plastic deformation: recent developments in evaluating the degree of homogeneity through the thickness of disks processed by high-pressure torsion*. J Mater Sci, 2012. **47**: p. 7719-7725
- [13] S.Khamsuk, Nokeun Park, Hiroki Adachi, Daisuke Terada, Nobuhiro Tsuji, *Evolution of ultrafine microstructures in commercial purity aluminum heavily deformed by torsion*. J Mater Sci, 2012. **47**: p. 7841-7847
- [14] G.R. Canova, U.F. Kocks, J.J.Jonas, *Theory of torsion texture development*. Acta Metall., 1984. **32(2)**: p. 211-226
- [15] F.Monthellet, M.Cohen, J.J.Jonas, *Axial stresses and texture development during the torsion testing of al, cu and a-fe*. Acta metall., 1984. **32 (11)**: p. 2077-2089
- [16] Jiuwen Zhang, Nong Gao, Marco J. Starink, *Microstructure development and hardening during high pressure torsion of commercially pure aluminium: Strain reversal experiments and a dislocation based mode*. Materials Science and Engineering A, 2011. **528(6)**: p. 2581-2591
- [17] D.Orlov, Yoshikazu Todaka, Minoru Umemoto, Nobuhiro Tsuji, *Role of strain reversal in grain refinement by severe plastic deformation*. Materials Science and Engineering A, 2009. **499**: p. 427-433
- [18] Hyoung Seop Kim, *Finite element analysis of high pressure torsion processing*. Journal of Materials Processing Technology, 2001. **113 (1-3)**: p 617-621
- [19] Megumi Kawasaki, Terence G. Landgon, *The significance of strain reversals during processing by high-pressure torsion*. Materials Science and Engineering A, 2008. **498(1-2)**: p. 341-348
- [20] L.S. Toth, J.J.Jonas, D. Daniel, J.A.Bailey, *Texture development and length changes in copper bars subjected to free end torsion*. Textures and Microstructures, 1992. **19**: p. 245-262
- [21] Aicha Loucif, Thierry Baudin, Francois Brisset, Roberto B.Figueiredo, Rafik Chemam, Terence G. Langdon, *An investigation of microtexture evolution in an AlMgSi alloy processed by high-pressure torsion*. Materials Science Forum, 2012. **702-703**: p.165-168
- [22] Bay, B., et al., *Overview No-96 - Evolution of Fcc Deformation Structures in Polyslip*. Acta Metallurgica Et Materialia, 1992. **40(2)**: p. 205-219
- [23] Hughes, D.A. and N. Hansen, *High angle boundaries formed by grain subdivision mechanisms*. Acta Materialia, 1997. **45(9)**: p. 3871-3886.
- [24] C.T. Young et al., *Dislocation substructures formed during the flow stress recovery of high purity aluminium*. Materials Science and Engineering, 1986. **81**: p. 391-407

- [25] B.Bay et al., *Deformation structures in lightly rolled pure aluminium*, Materials Science and Engineering A, 1989. **113**: p. 385-397
- [26] Y. Ito, Z. Horita, *Microstructural evolution in pure aluminum processed by high-pressure torsion*, Materials Science and Engineering, 2009. **503**: p. 32–36
- [27] T. Hasegawa, T. Yakou, S. Karashima, *Deformation behavior and dislocation structures upon stress reversal in polycrystalline aluminium*. Materials Science and Engineering. 1975, **20**: p. 267–276
- [28] J.Gubicza, N.Q.Chinh, Z.Horita, T.G Langdon, *Effect of Mg addition on microstructure and mechanical properties of aluminium*. Mater.Sci.Eng.A, 2004, **387**: p. 55–59.
- [29] Z. Horita, T.G. Langdon, *Microstructures and microhardness of an aluminum alloy and pure copper after processing by high-pressure torsion*. Materials Science and Engineering A, 2005. **410–411**: p. 422–425.
- [30] Megumi Kawasaki, Byungmin Ahn, Terence G.Langdon, *Effect of strain reversals on the processing of high-purity aluminum by high-pressure torsion*. J.Mater Sci, 2010. **45**: p. 4583-4593.
- [31] Dmitry Orlov et al., *Reversal straining to manage structure in pure aluminum under SPD*. Materials Science Forum, 2008. **584-586**: p. 133-138
- [32] P. Gilormini., et al., *Reference ODF calculations for the torsion Of fcc rate sensitive polycrystals*. Textures and Microstructures, 1991. **14-18**: p. 1197-1202
- [33] A.P. Zhilyaev et al., *An examination of microtexture and microstructure in ultrafine-grained nickel*. Mater.Sci., 2004. **7**: p. 41-49